Effect of aerosols on the downward shortwave irradiances at the surface: Measurements versus calculations with MODTRAN4.1

J. S. Henzing, W. H. Knap, and P. Stammes
Royal Netherlands Meteorological Institute (KNMI), De Bilt, Netherlands

A. Apituley, J. B. Bergwerff, and D. P. J. Swart
National Institute for Public Health and the Environment (RIVM), Bilthoven, Netherlands

G. P. A. Kos and H. M. ten Brink
Energy Research Centre of the Netherlands (ECN), Petten, Netherlands

Received 9 September 2003; revised 28 April 2004; accepted 14 May 2004; published 28 July 2004.

[1] A detailed analysis of measurements and model calculations of clear-sky shortwave irradiances at the surface is presented for a set of 18 cases collected during 3 cloudless days in the Netherlands in 2000. The analysis is focused on the influence of the optical and physical properties of aerosols on simulations of direct and diffuse downward solar irradiance at the surface. The properties of aerosols in the boundary layer are derived from surface measurements, under the assumption that all aerosol is confined to a well-mixed atmospheric boundary layer. The simulations of the irradiances are performed with the radiative transfer model MODTRAN 4, version 1.1. The analysis reveals no discernable differences between model and measurement for the direct irradiance, but several significant differences for the diffuse irradiance. The model always overestimates the diffuse irradiance measurements by 7 to 44 Wm^{-2} (average: 25 Wm^{-2}). On the basis of an estimated uncertainty in the differences of 18 Wm^{-2}, it appears that for 13 out of 18 cases the model significantly overestimates the measurements. This number decreases if instrumental errors (e.g., pyranometer zero-offset) and assumptions on the model input (e.g., wavelength-independent surface albedo) are considered. Nevertheless, the analysis presented here points to a persistent and significant positive model-measurement difference for the diffuse irradiance, which typically amounts to 1–4% of the top-of-atmosphere irradiance, and does not depend on the solar zenith angle. The reason for the discrepancy may be found in the presence of ultrafine absorbing aerosol particles that were not detected by the surface instrument for measuring aerosol absorption. It is also possible that these particles are not present near the surface, due to dry deposition, but do contribute to the total extinction if they are situated higher up in the boundary layer. *INDEX TERMS:* 0305 Atmospheric Composition and Structure: Aerosols and particles (0345, 4801); 0345 Atmospheric Composition and Structure: Pollution—urban and regional (0305); 0360 Atmospheric Composition and Structure: Transmission and scattering of radiation; 1610 Global Change: Atmosphere (0315, 0325); *KEYWORDS:* aerosol-radiation interaction, shortwave closure

Citation: Henzing, J. S., W. H. Knap, P. Stammes, A. Apituley, J. B. Bergwerff, D. P. J. Swart, G. P. A. Kos, and H. M. ten Brink (2004), Effect of aerosols on the downward shortwave irradiances at the surface: Measurements versus calculations with MODTRAN4.1, *J. Geophys. Res.*, *109*, D14204, doi:10.1029/2003JD004142.

1. Introduction

[2] Atmospheric circulation is primarily governed by the distribution of incoming solar radiation. The theoretical understanding of radiative transfer is therefore of crucial importance when studying weather, climate, or changes in climate. The idea that radiation modeling has a well established physical basis is widespread in the climate community. However, using 26 models of various degrees of sophistication, the international program of Intercomparison of Radiation Codes Used in Climate Models (ICRCCM) revealed a considerable spread in the radiative response to same input atmospheric profiles for 57 cases considered [*Fouquart et al.*, 1991]. After considerable effort throughout the 1990s, the spread in model results of radiation codes is still substantial. Using a selection of four (midlatitude summer) cloud- and aerosol-free ICRCCM standard cases in eight different models, *Kinne et al.* [1998] find differences in modeled solar broadband irradiances at the surface up to 25 Wm^{-2} at solar zenith angles of 30°. The most recent ICRCCM extension [*Barker et al.*,

0148-0227/04/2003JD004142$09.00

2003] focuses on the performance of one-dimensional solar radiative transfer codes when operating on partially cloudy atmospheres. The single clear-sky case considered in this study reveals that the striking underestimated atmospheric absorption (20 Wm^{-2} for overhead Sun and standard tropical atmosphere) is only slightly less than found in studies performed 10–15 years ago.

[3] Convergence of model results is desirable, but it is absolutely necessary that models and observations agree on the distribution of solar energy in the atmosphere. *Cess et al.* [1996], *Conant et al.* [1997, 1998], *Valero and Bush* [1999], and *Li and Moreau* [1996] find agreement between observed and calculated atmospheric shortwave absorption for cloud-free situations, but others report poor agreement on the amount of energy absorbed by both the cloudy atmosphere [*Cess et al.*, 1995; *Ramanathan et al.*, 1995; *Pilewskie and Valero*, 1995] and the relatively simple cloud-free atmosphere [*Wild et al.*, 1995; *Arking*, 1996, 1999a, 1999b; *Charlock and Alberta*, 1996; *Kato et al.*, 1997; *Kinne et al.*, 1998; *Halthore et al.*, 1998; *Wild*, 1999; *Halthore and Schwartz*, 2000; *Wendisch et al.*, 2002]. These latter cloud-free studies reveal that, on a global scale, observed absorption in the atmosphere is typically 10–30 Wm^{-2} larger than predicted by radiative transfer models. Differences are largest at low latitudes year round and for midlatitude summers, with modeled absorption up to 50 Wm^{-2} larger than measured. However, the bulk of the differences found is between 20 and 35 Wm^{-2}.

[4] In this study we investigate the role aerosols play in this model-measurement discrepancy. To do so, we choose to compare measured and modeled incoming solar broadband direct and diffuse irradiances at the surface into great detail on a limited number of cloudless days. The calculations are performed with the state-of-the-art radiative transfer code MODTRAN4.1 [*Berk et al.*, 2000, and references therein]. The input parameters used to run the model (aerosol optical thickness, aerosol absorption, and scattering coefficients including relative humidity dependence, aerosol asymmetry parameter, boundary layer height, water vapor, ozone, and meteorological parameters) are obtained from comprehensive field observations during CLOSAeR. The CLOSAeR project was carried out in the framework of the Dutch National Research Programme on Global Air Pollution and Climate Change. The project aimed to study the effects of aerosol on closure of the regional short-wave radiation balance in the Netherlands in 2000 [*Henzing et al.*, 2001].

[5] Our study together with the LACE98 field campaign [*Ansmann et al.*, 2002; *Wendisch et al.*, 2002] are, to our knowledge, the only radiation closure studies performed in Europe. In the study of Wendisch et al., aerosol optical properties are obtained from Mie theory using measured microphysics, refractive index, and humidity particle growth. In our study we choose not to calculate the aerosol optical properties but to obtain these properties independently from measurements, as was done, for example, by *Halthore and Schwartz* [2000]. The advantage of this method is that sensitivities to model input parameters can be added. Moreover, we avoid that a measurement error in a single quantity propagates into all model input parameters. Another important feature of our study is that the selection of days is such that there are no layers with raised aerosol concentration above the boundary layer. We therefore assume that all aerosols are contained within the rapidly overturning boundary layer [*Veefkind et al.*, 1996]. In this way aerosol characteristics measured at the surface provide valuable information on the vertical dependence of aerosol optical properties, that are used to obtain boundary layer averaged aerosol scattering and absorption coefficients.

[6] In section 2 we present the experimental approach and we give an overview of the used set of instruments. In section 3 we discuss the radiation instruments and their measurement errors. The model and its input parameters are presented in section 4. In section 5 the errors in the model calculations are estimated from the model input parameter errors. The actual model-measurement comparison is done in section 6. In section 7, results are discussed. Conclusions are given in section 8.

2. Experimental Approach

[7] We study the effect of aerosols on shortwave surface irradiances on completely cloudless days. The reason for this restriction is threefold. First, the effect of aerosols on radiative transfer is best investigated when their effect is isolated, that is when all other contributions are well known. Second, Sun photometers cannot easily distinguish cloud optical thickness from aerosol optical thickness. Third, reflections from clouds would affect the amount of diffuse radiation received.

[8] Cloudless days are very rare in the Netherlands. In order to use all cloudless days in the year 2000, a standby warning was issued to the people that were responsible for the instruments that required manual operation or surveillance when the weather forecast was promising, so that crucial instruments would actually be operating. During the measurement days the absence of thin stratus or cirrus clouds was verified by visual inspection. Finally, the absence of clouds not visible to the naked eye was verified with lidars. However, we cannot exclude the presence of clouds away from zenith with certainty since the lidars only sample the zenith direction. In section 2.1 we discuss how lidars are used for the selection of cloudless days. In section 2.2 the instruments that are actually used in the model-measurement comparison are described and discussed. The instruments were deployed in the center of the Netherlands at two locations less than 2 km apart, De Bilt (52.100°N, 5.183°E) and Bilthoven (52.120°N, 5.196°E), unless stated otherwise (Figure 1). All instruments are listed in Table 1.

2.1. Selection of Cloudless Days

[9] We use a troposphere lidar to detect clouds in the altitude range of 1 to 15 km [*Sunesson et al.*, 1994; *Apituley et al.*, 1997]. A boundary layer lidar routinely profiles the lowest 4 km of the atmosphere. When the lidars detect a cloud, the measurement day is excluded. Furthermore, the boundary layer lidar provides the height of the planetary boundary layer [*Van Pul et al.*, 1994].

[10] Sometimes high aerosol concentrations above the boundary layer are present. These so-called residual layers usually occur in the altitude range up to 3 km, and consist of aged polluted air masses transported on a continental scale. As a result of the growth of the boundary layer during the

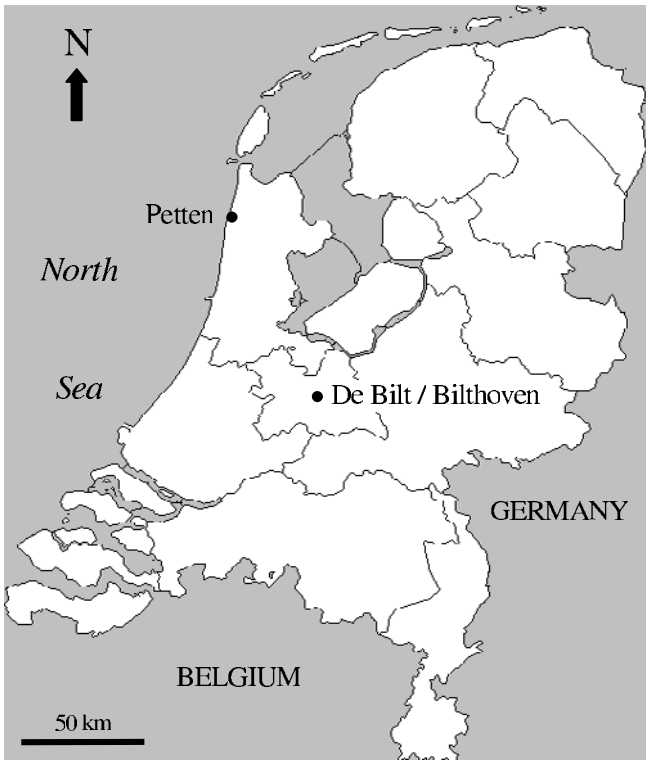

Figure 1. The Netherlands with the measuring site De Bilt/Bilthoven in the center.

day, the lowest nocturnal residual layers are often completely mixed into the boundary layer. Lidar data clearly mark the moment of mixing. The boundary layer lidar, measuring atmospheric backscatter, cannot discriminate between thin clouds and high aerosol concentrations. High aerosol concentrations above the boundary layer are seen as clouds and the measuring day is therefore excluded. Consequently, the lidar check does not only confirm the absence of clouds, but it also ascertains that no residual layers are present above the boundary layer.

[11] Following this approach, we select 3 cloudless days: 5 May, 14 May, and 19 June 2000. Nocturnal surface inversion layers and low level residual layers are cleared away by shallow convective overturning at about 14.00, 10.00, and 12.45 UT for 5 May, 14 May, and 19 June, respectively. The well-mixed surface aerosol layer found at later times, clearly indentified by steady increase in radiosonde relative humidity with increasing height (Figure 2), was used in our study.

2.2. Instrumentation

[12] In addition to the lidars that are used for the selection of cloudless measurement days, we use two types of instruments. The first type of instruments measures solar radiation. Solar broadband direct and diffuse surface solar irradiances are measured on a routine basis with a pyrheliometer and a shaded pyranometer, respectively.

[13] The second type of instruments provides the atmospheric input data needed for the radiative transfer model calculations. The main quantities here are the aerosol optical properties. The spectral aerosol optical thickness is obtained from a six-channel Sun photometer. The aerosol absorption coefficient is deduced from measurements with a standard commercial instrument that measures light-absorption (aethalometer). The aerosol light scattering coefficient is determined with (integrating) nephelometers. The sum of scattering and absorption coefficients defines the extinction coefficient. The aerosol single scattering albedo is defined as the fraction of extinction that is caused by scattering. The effect of water vapor on the scattering properties of aerosols is taken into account in the single scattering albedo using a radiosonde water vapor profile together with the relative-humidity dependence of the light-scattering as measured with a humidograph [*Ten Brink et al.*, 2001]. The asymmetry parameter of aerosols is not measured on site. However, the asymmetry parameter can be assessed using Mie theory and simultaneous aerosol size distribution measurements made in Petten, situated 80 km to the northwest (downwind) of Bilthoven/De Bilt. The mixing height of the boundary layer is measured with the boundary layer lidar. The water vapor column is obtained from vertically integrated radiosonde data. The solar broadband surface albedo of the area surrounding Bilthoven/De Bilt is obtained from AVHRR satellite data. The total ozone column above the measuring site is measured with a Brewer spectrometer.

3. Surface Irradiance Measurements

[14] Irradiance, E, is the radiative energy flux per unit time in a given wavelength interval through a horizontal surface of unit area. The irradiance is obtained by integrating the radiance, the radiative power per unit solid angle in a particular direction, weighted with the cosine of the viewing zenith angle, $\mu = \cos\theta$, over all viewing directions in a

Table 1. Overview of Instrumentation and Way of Operation

Location	Instrument	Operator	Parameters	Operation
Bilthoven	Boundary Layer Lidar	RIVM	PBL height, backscatter profile	automatic
	Tropospheric UV lidar	RIVM	backscatter profile, aerosol extinction profile	operator controlled
	Aethalometer 1	RIVM	aerosol absorption coefficient	automatic
	Aethalometer 2	RIVM	aerosol absorption coefficient	automatic
	Nephelometer	ECN	aerosol scattering coefficient	automatic
De Bilt	Sun photometer	KNMI	aerosol optical thickness	automatic
	Pyrheliometer	KNMI	direct irradiance	automatic
	Pyranometer	KNMI	diffuse irradiance	automatic
	Radiosonde	KNMI	water vapor column, relative humidity	manual
	Brewer spectrometer	KNMI	ozone column	automatic
Petten	Impactor	ECN	aerosol size distribution, composition	manual

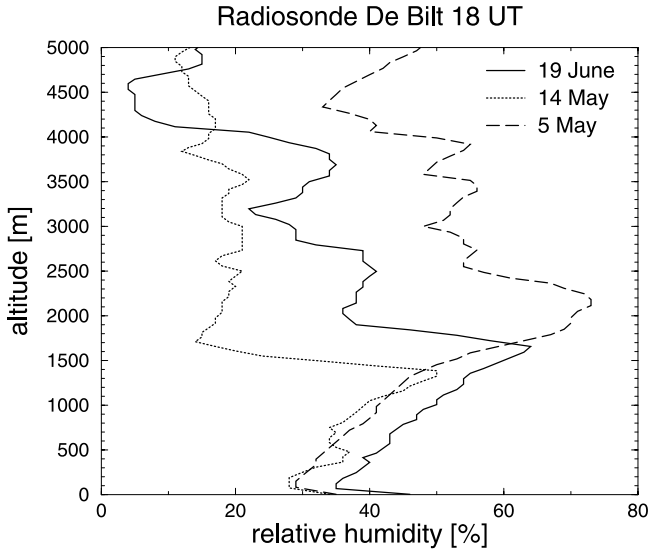

Figure 2. Radiosonde relative humidity profiles for 5 May, 14 May, and 19 June 2000. Relative humidity steadily increases from the surface, indicating that the boundary layer is well-mixed, until a sharp decrease occurs in relative humidity which marks the top of the boundary layer.

hemisphere of 2π steradians. The irradiance is a function of wavelength: $E(\lambda)$, with the unit [Wm^{-2} nm^{-1}]. Since we will mainly use spectrally integrated irradiances, we define:

$$E = \int_{250\ \mathrm{nm}}^{5000\ \mathrm{nm}} E(\lambda)d\lambda, \tag{1}$$

with the unit [Wm^{-2}]. The downward solar irradiance at the surface is often called the global irradiance, denoted by E_{glo}. It is useful to separate the downward irradiance at the surface in a direct part (unscattered radiation) and a diffuse part (scattered radiation), denoted by E_{dir} and E_{dif}, respectively. So, we have at the surface:

$$E_{glo} = E_{dir} + E_{dif}. \tag{2}$$

The direct irradiance measured perpendicular to the solar beam is called DNSI (direct normal solar irradiance). At the surface DNSI equals E_{dir}/μ_0, where μ_0 is the cosine of solar zenith angle θ_0. The DNSI at top-of-atmosphere (TOA) is denoted by E_0.

3.1. Direct Irradiance

[15] Direct downward irradiance is measured on a routine basis with a Kipp & Zonen CH1 pyrheliometer placed on a fully automatic Sun tracker. At the Royal Netherlands Meteorological Institute (KNMI), routine monitoring instruments are connected to standardized data acquisition systems that amplify the output voltage and convert the signal to the appropriate unit. The data acquisition system takes 12-s samples, which are averaged to 10-min mean values that are used in this study. The pyrheliometer measures DNSI received within a 5° field of view. DNSI is converted into direct solar irradiance by using the solar zenith angle.

[16] Forward scattered light within the field of view of the pyrheliometer is unjustly considered direct irradiance. We estimate the amount of diffuse irradiance due to molecular and particle scattering from the work of *Box and Deepak* [1979, equation (19)] and *Deepak and Box* [1978a, 1978b]. Using 19 June 2000 aerosol optical thickness, phase function, and solar zenith angle, we find diffuse/direct fractions at 500 nm that we apply to the whole spectrum. Doing that, we find 1.4 and 1.6 Wm^{-2} diffuse irradiance contribution in the pyrheliometer measurement for 12:30 and 15:30 UT, respectively.

[17] The sensor in combination with a filter determines the spectral response and spectral range of the pyrheliometer. The sensor is a thermal detector with an essentially flat spectral response from 0 to 50 μm. The filter, which protects the blackened thermopile against weathering, is an infrasil I window of 2 mm thickness with a spectral range of 0.2 to 4 μm.

[18] Using the Sun as a source, the pyrheliometer is calibrated directly to the World Standard Group (WSG) in Davos, Switzerland, which maintains the World Radiometric Reference (WRR) [*Fröhlich*, 1991; *Fröhlich et al.*, 1995]. The WRR comprises seven absolute cavity radiometers that ensure high absorptivity over the spectral range of interest for solar radiometry. This means that, although the CH1 pyrheliometer does not see solar radiation beyond the cutoff of the infrasil window (4 micron), this part is included by reference to the reading of the WSG. The pyrheliometer in our study thus measures the total solar spectrum.

[19] In terms of the ISO 9060 standard, which has been accepted by the *World Meteorological Organization* (*WMO*) [1983], the CH1 is a "first class" pyrheliometer. The largest source of error in our pyrheliometer measurements is caused by the temperature dependency of the thermocouple material. The maximum deviation, relative to 20°C output signal, over the range [−20°C, 50°C] is estimated to be 8 Wm^{-2} at a cloudless solar noon in spring. The estimated uncertainties in pyrheliometer measurements are given in Table 2. For a complete discussion on the error associated with the pyrheliometer used in this study the reader is referred to *Henzing and Knap* [2001]. The measurements of direct irradiance for the 3 selected cloudless days are presented in Figure 4.

3.2. Diffuse Irradiance

[20] The diffuse downward irradiance is measured on a routine basis with a shaded Kipp & Zonen CM11 pyranometer. The pyranometer is placed on the same Sun tracker as the pyrheliometer. A shading sphere is fixed on the platform in such a way that the shading cone of the pyranometer is identical to the field of view of the pyrheliometer.

[21] From section 3.1 we estimate the missing diffuse irradiance for 19 June 2000 at 1.4 and 1.6 Wm^{-2} for 12:30 and 15:30 UT, respectively. As for the direct irradiance, only 10-min mean values of the diffuse irradiances are available.

[22] The thermal detector of the pyranometer is easily affected by wind, rain, and thermal radiation losses to the environment. Therefore two Schott K5 glass domes, of 2 mm thickness each, shield the detector. The spectral range of the pyranometer is limited by the transmission of the glass; the 50% points are 335 nm and 2800 nm.

[23] The pyranometer is calibrated at KNMI against the KNMI standard pyranometer using a lamp. The standard

Table 2. Errors in Measured and Modeled Irradiances, and the Combination of Both[a]

Irradiance	Error Measurement	Error Calculation		Error Combination	
		12:30 UT	15:30 UT	12:30 UT	15:30 UT
E_{dir}	10	12	10	16	14
E_{dif}	7	17	17	18	18
$E_{dir} + E_{dif} = E_{glo}$	12	17	16	21	20
$E_{\uparrow,\mathrm{TOA}}$	...	22	15	...	...
E_{abs}	...	30	25	...	...

[a]Units are in Wm^{-2}. Error measurement: Pyrheliometer (E_{dir}) and pyranometer (E_{dif}) instrumental errors [*Henzing and Knap*, 2001]. Global irradiance is obtained by taking the sum of direct and diffuse irradiances ($E_{dir} + E_{dif}$). Error calculation: Error in MODTRAN4 model-calculated irradiances due to errors in model input parameters at two reference times on 19 June 2000 as explained in section 5. Error combination: Combined error in calculations and measurements as explained in section 6. All errors are positive and negative with equal probability.

pyranometer was calibrated at the World Radiation Centre (WRC) in Davos according to the component summation method [*WMO*, 1996]. In this method the pyranometer to be calibrated is operated unshaded. The output voltage of the pyranometer is then linked to the incident solar irradiance. The direct irradiance is determined using the WSG and the diffuse irradiance is measured using the shaded standard pyranometer of the WRC as stated in the WMO technical regulations. Both direct (WSG) and diffuse (WRC) standards measure the total solar range, so that the shaded pyranometer used in this study also yields results for the total solar range despite the spectral selection of the glass domes [*Fröhlich et al.*, 1995].

[24] A critical shortcoming of pyranometers is the existence of a zero offset. The pyranometer reads a zero offset, which is a voltage that is not caused by the absorption of solar radiation. Zero offset is mostly caused by the disturbance of the thermal equilibrium within the instruments. Longwave cooling of the pyranometer glass domes is the major source of zero offset for pyranometers under stable temperature conditions. Zero offset caused by longwave cooling of the domes is most easily recognized during the night in the absence of solar irradiance. The zero offset then leads to the well-known negative pyranometer readings.

[25] It is unlikely that simple interpolations or extrapolations of nighttime offsets can be used to estimate daytime offsets and correct the measurements [*Cess et al.*, 2000; *Bush et al.*, 2000]. Other surrogate methods to estimate the magnitude of daytime offsets are (1) use of the temperature difference between the sensor and the dome [*Bush et al.*, 2000], or (2) use of the net longwave downward irradiance as measured by an up looking pyrgeometer [*Dutton et al.*, 2001; *Halthore and Schwartz*, 2000]. These methods were not applicable here, because method 1 requires instrument modification and method 2 requires pyrgeometer measurements that were not available on site.

[26] In view of the fact that an accurate nighttime-to-daytime extrapolation is not trivial, and because pyranometer dome temperatures and longwave downward radiation were not measured, it was decided not to correct the pyranometer measurements for possible thermal zero-offsets, rather than applying an uncertain correction. Nevertheless, in section 6.5.3, a first-order estimate of the daytime offset is given in view of the model-measurement intercomparison of irradiances.

[27] The error in shaded pyranometer measurements is discussed by *Henzing and Knap* [2001] and given in Table 2. Table 2 contains the uncertainties in the irradiance measurements (as estimated by *Henzing and Knap* [2001]), in the model calculations (due to uncertainties in measured model input parameters, to be discussed in section 5), and the combination of both uncertainties (section 6). The measurements of diffuse irradiance for the 3 selected cloudless days are presented in Figure 4.

3.3. Global Irradiance

[28] Global irradiance can be measured with unshaded pyranometers. However, these measurements may suffer from relatively large errors due to the irregular cosine and azimuth response of the pyranometer. For measuring global irradiance the best accuracy is obtained by taking the sum of direct irradiance measured with a pyrheliometer (E_{dir}) and diffuse irradiance measured with a shaded pyranometer (E_{dif}) [*Flowers and Maxwell*, 1985; *Ohmura et al.*, 1998; *Wardle et al.*, 1996; *Michalsky et al.*, 1999]. We follow this approach. The global irradiances for the 3 selected cloudless days are presented in Figure 4.

[29] Despite the absence of cirrus and other thin clouds, the curves of the measured direct, diffuse, and global irradiances, as shown in Figure 4, are not very smooth, especially around noon. This typical behavior (for the Netherlands) is caused by irregular boundary layer growth. 19 June, around 14 UT, direct irradiance is significantly lower than at adjacent times whereas diffuse irradiance is higher by about the same amount. Most probably, this increased extinction (scattering) is caused by a peak in the aerosol load as there is no significant change in the Angström parameter.

4. Radiative Transfer Model and Its Input Data

4.1. MODTRAN4.1 Description

[30] For the calculation of irradiances we use the MODTRAN4 code (version 1.1, 17 April 2000) [see *Berk et al.*, 2000, and references therein]. MODTRAN4 is a spectral band radiative transfer model with a moderate spectral resolution (down to 2 cm^{-1}). This is sufficient for our purpose of obtaining the spectrally integrated solar irradiance. In order to calculate molecular absorption in the presence of multiple scattering accurately, we use the correlated-k treatment using 17 absorption coefficients (k-values) per spectral bin of 1 cm^{-1}. Multiple scattering in MODTRAN4 is based on the use of multiple streams in the discrete-ordinates method (disort code of *Stamnes et al.* [1988]); here we use 8 streams. The only missing element in MODTRAN4 is polarization. However, for irradiances the

neglect of polarization yields only a very small error, far below 1% for the spectral range of interest here [*Lacis et al.*, 1998].

4.2. Overview of Required Input Data

[31] Atmospheric radiation modeling requires an adequate description of the incoming solar irradiance, the thermal structure of the atmosphere, the surface reflectance, and the composition and vertical profiles of atmospheric constituents (gases and aerosols). The optical ingredients of our model atmosphere are given below.

4.2.1. Solar Irradiance

[32] For the top-of-atmosphere solar irradiance we use the MODTRAN built-in *Kurucz* [1995] spectral irradiance data file, that integrates to $E_0 = 1368$ Wm^{-2} at 1 astronomical unit. Scaling of the solar irradiance accounts for the varying Earth-to-Sun distance throughout the year.

4.2.2. Gases and Thermal Structure

[33] The *Anderson et al.* [1986] database describing the thermal and gaseous constituent profiles is incorporated into MODTRAN. In this study the standard midlatitude summer profiles of the database are used. The profiles of H_2O and O_3 are scaled with the measured column densities. For CO_2 the volume mixing ratio of 365 ppmv as recommended by the *Intergovernmental Panel on Climate Change* (*IPCC*) [2001] is used for the scaling. The midlatitude summer reference pressure of 1013 hPa is used as the surface pressure. The use of the actual surface pressure, being 1013, 1021, and 1015 hPa on the respective measuring days 5 May, 14 May, and 19 June 2000, would only lead to minor modification in the Rayleigh scattering (less than 0.5 Wm^{-2}). The profiles of NO_2, CO, CH_4, and 25 less radiatively active species are used unchanged.

4.2.3. Surface Albedo

[34] The surface albedo used in our MODTRAN calculations is spectrally flat. The actual surface albedo, however, has a wavelength dependence that is a function of surface type. To account for this wavelength dependence, while using a constant albedo, we weigh the spectral surface reflectance with modeled incoming global irradiance as will be explained in section 4.3.7. The consequence of this simplification is discussed in section 6.5.2.

4.2.4. Aerosol Characteristics

[35] In general, aerosol concentrations in the free troposphere and stratosphere are much lower than in the boundary layer. In the absence of aerosol-rich residual layers (see section 2.1) the total aerosol optical thickness is therefore very likely dominated by aerosol scattering and absorption in the boundary layer [*Veefkind et al.*, 1996]. Therefore we confine the aerosols in the model to the boundary layer. The height of the boundary layer, H_{bl}, was measured with a lidar. To represent the optical properties of the aerosols, we specify the extinction optical thickness, τ_{aer}, the single scattering albedo, a_{aer}, and the asymmetry parameter, g.

[36] Aerosols of various chemical compositions and with different shapes and sizes are usually externally and internally mixed. We assume that this aerosol mixture can be regarded as an ensemble and that the scattering and absorption properties of this ensemble are determined by an average aerosol particle. The scattering cross section of this ensemble average aerosol particle is denoted as: C_{sca} [m^2]. Its absorption cross section is denoted as: C_{abs} [m^2]. The aerosol particle number density of the volume element is denoted by n [m^{-3}]. The scattering coefficient, k_{sca} [m^{-1}], of the ensemble can then be defined as:

$$k_{sca}(z) = n(z)C_{sca}(z). \tag{3}$$

Likewise, the absorption coefficient, k_{abs} [m^{-1}], is defined as:

$$k_{abs}(z) = n(z)C_{abs}(z). \tag{4}$$

Owing to rapid vertical mixing within the boundary layer on the selected days, the aerosol composition aloft in the boundary layer and the ensemble at the ground should strongly resemble each other. Changes in the scattering coefficient and absorption coefficient are caused by expansion of the volume element during uplift (n will decrease) and by water uptake of the aerosols due to increasing ambient relative humidity during uplift (C_{sca} and C_{abs} will increase). The decrease in aerosol particle number density with increasing altitude is linearly proportional to the decrease in air density with increasing altitude. A humidification factor, f(RH) (i.e., the change in particle scattering or absorption due to water uptake by the particles) measured at the ground in combination with the relative humidity at a certain altitude yields the multiplication factor for the aerosol cross sections at that height.

[37] Including the aerosol water uptake and volume expansion, we obtain the boundary layer average scattering coefficient, $\overline{k_{sca}}$, and absorption coefficient, $\overline{k_{abs}}$:

$$\overline{k_i} = \frac{1}{H_{bl}} \int_{z=0}^{z=H_{bl}} k_i(z=0) \frac{\rho(z)}{\rho_0} f(RH(z)) dz, \tag{5}$$

where z is the height, i stands for scattering or absorption, $\rho(z)$ is the density of air at altitude z, and ρ_0 the density of air at the ground. Multiplying these coefficients with the boundary layer height yields the boundary layer aerosol scattering optical thickness, τ_{sca}^{bl}, and the boundary layer aerosol absorption optical thickness, τ_{abs}^{bl}, respectively,

$$\tau_i^{bl} = H_{bl}\overline{k_i}. \tag{6}$$

Because extinction is the sum of scattering and absorption, the boundary layer aerosol (extinction) optical thickness reads:

$$\tau_{ext}^{bl} = \tau_{sca}^{bl} + \tau_{abs}^{bl}. \tag{7}$$

The (extinction) aerosol optical thickness of the total atmosphere, τ_{aer}, is always greater than the aerosol optical thickness of the boundary layer, τ_{ext}^{bl}, since aerosols are also present in the free atmosphere above the boundary layer. However, on the measurement days, extinction in the free atmosphere is expected to be small due to the absence of (aerosol rich) residual layers. Therefore we assume in our study that all aerosols are in the boundary layer. The value of the measured τ_{aer} is thus assigned to the boundary layer and plays the role of τ_{ext}^{bl}

$$\tau_{aer} = \tau_{ext}^{bl}. \tag{8}$$

Below it is explained how the spectral aerosol optical thickness, $\tau_{aer}(\lambda)$, is obtained from measurements.

[38] The aerosol single scattering albedo, a_{aer}, is the ratio between scattering and the sum of scattering and absorption. It expresses the chance that a scattered photon is not absorbed but will continue its journey as diffuse light. As we assume that all aerosols are confined to the boundary layer, we can define:

$$a_{aer} = \frac{\overline{k_{sca}}}{\overline{k_{sca}} + \overline{k_{abs}}}. \quad (9)$$

How to obtain the boundary layer average absorption and scattering coefficients from measurements will be explained in sections 4.3.2 and 4.3.3, respectively. In section 4.3.4 it will be explained how the asymmetry parameter is obtained.

4.3. Measurements of Model Input Data

4.3.1. Spectral Aerosol Optical Thickness

[39] The spectral aerosol optical thickness is measured with the SPUV Sun photometer placed on a Sun tracker. The SPUV (YES, Inc.) measures the direct solar spectral irradiance at 368, 500, 670, 780, 870, and 940 nm. The SPUV is designed according to the WMO recommendations for Sun photometers [*Fröhlich and London*, 1986]. The 940 nm (water vapor) channel is not used in this study. The SPUV has been calibrated using the Langley method [*Harrison and Michalsky*, 1994]. For the calibration, 22 cloudless mornings and afternoons in the 3 years preceding our study were used (for details, see *Henzing and Knap* [2001]). Absolute calibration of the SPUV makes it possible to find the atmospheric optical thickness for a single clear-sky event and to determine its variation during the day. The atmospheric optical thickness is caused by molecular scattering, gaseous absorption, and aerosol scattering and absorption. The first five SPUV channels are outside major absorption bands. For this reason aerosol optical thickness can be deduced by subtracting the Rayleigh scattering and ozone absorption (Chappuis band) optical thickness from the total atmospheric optical thickness. In Figure 3 the aerosol optical thicknesses at 368, 500, and 870 nm are shown for the 3 selected days. The aerosol optical thicknesses at the five SPUV wavelengths are extrapolated to longer wavelengths to cover the entire solar spectrum. Using the Angström relationship, $\tau_{aer}(\lambda) = \beta\lambda^{-\alpha}$, the aerosol optical thicknesses at 1000, 1500, 2000, 3000, and 5000 nm are found. The aerosol optical thicknesses for all 10 wavelengths are used in the model calculations. In between these 10 wavelengths the aerosol optical thickness is linearly interpolated.

4.3.2. Aerosol Absorption Coefficient

[40] The absorption coefficient, k_{abs}, is measured with a ground-based aethalometer (Magee Scientific Corp, model AE-10-M). Details of the instrument and method of analysis are described by *Hansen and Schnell* [1991] and *Hansen* [2002]. The aethalometer is designed to measure the absorbing (black) fraction of the aerosol. The instrument collects the aerosol from ambient air on a quartz fiber filterband, while a continuous, calibrated airflow passes through it. The optical attenuation of light by the aerosol on the filterband is measured as a function of time, using a white light filament lamp and a photodetector at opposite sides of the band. The lamp and photodetector cover a wide spectral range. The exact range of the lamp is unknown and the detector is sensitive to wavelengths up to 1100 nm. The transmitted light intensity is measured and stored at 5-min intervals, and from the observed decrease in transmission and the known volume of the sampled air, the absorption coefficient is calculated. In this study the 5-min values are averaged to hourly mean values. The variation in light absorption due to water uptake by the particles is not measured and is assumed to be negligible. In section 5.2.3 we will show that the effect of the relative humidity dependence of the scattering coefficient is small due to low relative humidities at our comparison days. In general the humidity-sensitivity of the absorption coefficient is smaller than the humidity-dependence of the scattering coefficient. Therefore we use equation (5) with $f(\mathrm{RH}) = 1$ to calculate the average boundary layer aerosol absorption coefficient, $\overline{k_{abs}}$.

4.3.3. Aerosol Scattering Coefficient

[41] The aerosol scattering coefficient, k_{sca}, is determined with ground-based integrating nephelometers. The output of the instruments is the total scattering coefficient. After subtraction of the Rayleigh scattering contribution, the aerosol scattering coefficient is obtained. The effective wavelength of the instruments (Belfort Instruments MRI 1560) is 475 nm. The scattering coefficient at the measuring wavelength is translated to that at 500 nm using the Angström parameter as derived from Sun photometry.

[42] The standard procedure in nephelometry is to dry the air (including aerosol) by heating [*Ten Brink et al.*, 1996; *Dougle et al.*, 1998]. This avoids complications with uptake and loss of water by the hygroscopic aerosol components during sampling and protects the optics against condensation. To limit evaporative losses of semivolatile compounds such as ammonium nitrate, heating is limited to 40°C [*Dougle and Ten Brink*, 1996]. The measurement of the RH-dependence of the scattering coefficient, $f(\mathrm{RH})$, is performed in a humidograph [*Ten Brink et al.*, 2001]. The relative humidity profile is measured with a radiosonde at 6-hour intervals. Inserting the measurements of the nephelometers, the humidograph, and the radiosonde into equation (5) yields the boundary layer average scattering coefficient, $\overline{k_{sca}}$, which is used in this study.

[43] The single scattering albedo, a_{aer}, is obtained from $\overline{k_{sca}}$ and $\overline{k_{abs}}$ using equation (9). The thus obtained a_{aer} is valid at about 500 nm. Since multispectral measurements of $\overline{k_{sca}}$ and $\overline{k_{abs}}$ are not available, a_{aer} is assumed identical at all wavelengths.

4.3.4. Aerosol Asymmetry Parameter

[44] The asymmetry parameter of the aerosol is not measured in this study. However, the aerosol size distribution, resolved by eight size bins, was measured in Petten [*Henzing et al.*, 2001]. From the measured aerosol size distribution, the asymmetry parameter can be computed using Mie theory, assuming spherical particles. We use a Mie program [*De Rooij and Van der Stap*, 1984] assuming a lognormal size distribution with a median radius $r_g = 0.055$ micron and standard deviation $\sigma = 1.8$. We assume that the real part of the refractive index, $\mathrm{Re}(m)$, is 1.5 at all wavelengths. This is a typical value for water-soluble aerosols [*World Climate Program* (*WCP*), 1983]. The imaginary part, $\mathrm{Im}(m)$, is taken from water-soluble aerosol [*WCP*,

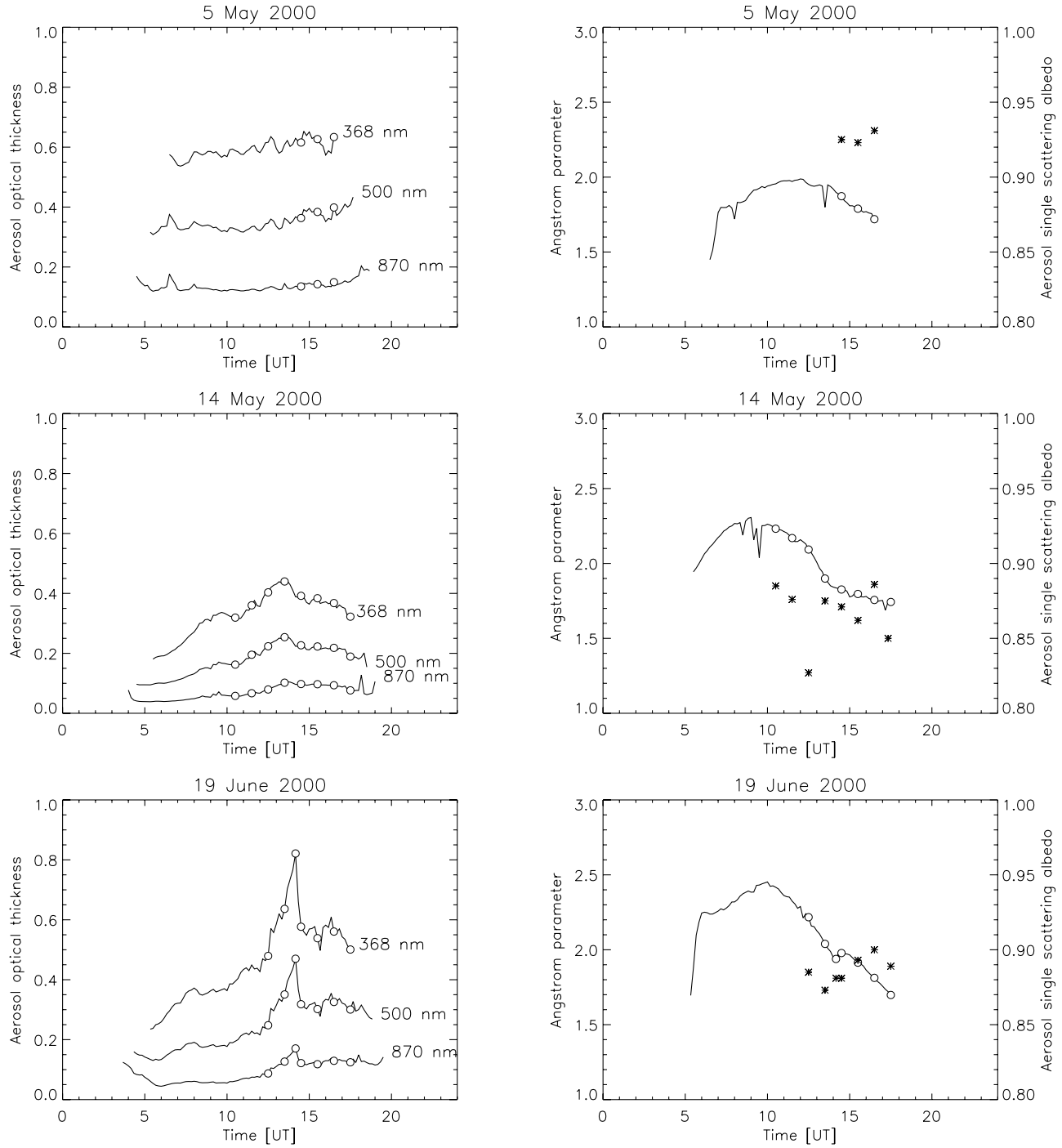

Figure 3. (left) Daily variation of the aerosol optical thickness at three wavelengths (368, 500, and 870 nm) for the 3 selected days; values used in calculations are indicated by open circles. (right) Daily variation of aerosol single scattering albedo (asterisks) and Angström parameter (lines, open circles), for the 3 selected days.

1983], but fixed to the average value of 0.01 in the near-IR. The results are tabulated in Table 3 for the selected wavelengths. It can be seen that g decreases rather strongly with increasing wavelength.

4.3.5. Water Vapor Column

[45] The effect of water vapor on the aerosol scattering properties is taken into account in the aerosol single scattering albedo (see section 4.2.4). Moreover, water vapor absorbs solar irradiance. The water vapor column is obtained from the vertically integrated radiosonde data, which are available every 6 hours. High temporal resolution integrated water vapor (IWV) measurements are available from a 50 km upwind station (Kootwijk, 5.81°E, 52.18°N) of a regional Global Positioning System (GPS) receiver network [*Klein Baltink et al.*, 2002]. Variations in IWV obtained using a linear interpolation between successive

Table 3. Results of Mie Calculations of Asymmetry Parameter g for Four Size Distributions (Lognormal, $\sigma = 1.8$)[a]

			Asymmetry Parameter g			
Wavelength, nm	Re(m)	Im(m)	r_g = 0.037 μm	r_g = 0.048 μm	r_g = 0.055 μm	r_g = 0.100 μm
368	1.5	0.005	0.624	0.659	0.674	0.703
501	1.5	0.005	0.567	0.615	0.638	0.694
675	1.5	0.006	0.496	0.557	0.588	0.674
780	1.5	0.010	0.457	0.524	0.558	0.661
870	1.5	0.010	0.426	0.496	0.533	0.647
1000	1.5	0.010	0.386	0.459	0.498	0.626
1500	1.5	0.010	0.269	0.342	0.385	0.546
2000	1.5	0.010	0.194	0.260	0.301	0.473
3000	1.5	0.010	0.112	0.160	0.194	0.357
5000	1.5	0.010	0.048	0.075	0.095	0.215

[a]Median radii r_g = 0.0368 μm and r_g = 0.0475 μm correspond to distributions for which the wavelength dependence of the extinction agrees with the Sun photometer data for 19 June 12:30 and 15:30 UT, respectively. r_g = 0.055 μm is the median radius used in the reference calculations. r_g = 0.1 μm corresponds to larger particles often observed (climatology in Petten).

radiosondes agreed very well with the variation in IWV values retrieved from the GPS network. For collocation reasons the interpolated radiosonde IWV data were used in our calculations.

4.3.6. Ozone Column

[46] The ozone column is measured with a Brewer spectrometer. Usually, the ozone column varies only slowly in the course of a day. The daily average value of the ozone column is therefore used in the calculations. For 5 May, 14 May, and 19 June 2000 we found, respectively, 360.4, 344.6, and 315.3 DU.

4.3.7. Surface Albedo

[47] Around the measuring site vegetation is dominant, but also motorways and built-up areas are found. To find a representative, but simple, spectral surface reflectance, we take a typical reflectance curve for photosynthetically active vegetation [*Bowker et al.*, 1985, Figure 2]. This spectrum is split into two regions, VIS and NIR, according to the main processes responsible for the behavior of the curve. In the visible region (VIS) with wavelengths smaller than 700 nm, reflectance is normally low especially in the growing season due to photosynthesis. The transition to the near infrared region (NIR) is marked with a sharp rise in the reflectance at about 700 nm (the red edge). Reflectance in the NIR is dominated by reflection at the cell walls and absorption by the leaf water content (beyond 1300 nm).

[48] In order to estimate the actual reflectances in the VIS/NIR, the NOAA/NASA Pathfinder AVHRR Land (PAL) data set was used (NASA, http://daac.gsfc.nasa.gov/, 2001). Of this data set, the so-called Daily Data Set was used, which contains global reflectances derived from AVHRR channels 1 and 2 mapped to an equal area projection (8 × 8 km^2). These reflectances (Table 4) are corrected for Rayleigh scattering and ozone absorption [*Agbu and James*, 1994]. AVHRR channel 1 (580−680 nm) and channel 2 (730−1100 nm) thus yield the reflectance in VIS (R_{VIS} = 0.08) and NIR (R_{NIR} = 0.22), respectively. Assuming a Lambertian surface, these reflectances equal surface albedos ($A_{s,VIS} = R_{VIS}$ and $A_{s,NIR} = R_{NIR}$). The shortwave broadband albedo (A_s) is obtained using a linear combination of the two reflectances:

$$A_s = c_{VIS}A_{s,VIS} + c_{NIR}A_{s,NIR}, \quad (10)$$

where the coefficients c_{VIS} and c_{NIR} represent the ratio of global irradiance at the surface in the relevant wavelength region to the shortwave broadband global irradiance. Using the reference MODTRAN calculations (see section 5) for the determination of the coefficients c_{VIS} and c_{NIR}, we find that A_s = 0.15 both at 12:30 UT and 15:30 UT.

5. Sensitivity Study of Model Calculations of the Clear-Sky Shortwave Irradiances

5.1. MODTRAN4.1 Calculations

[49] Calculations of the downward shortwave irradiances at the surface are performed for the selected 3 cloudless days 5 May, 14 May, and 19 June 2000 and presented in Figure 4. The calculations are performed for every hour for the periods that the boundary layer was well mixed, as long as the direct irradiance exceeded 150 Wm^{-2}. This results in a total of 18 cases. Because the entire solar spectrum is included in the irradiance measurements, simulated irradiances are integrated from 250 to 5000 nm. The pyrheliometer window and pyranometer domes shield the detectors from thermal radiation. Therefore thermal radiation is subtracted from the MODTRAN calculated irradiances. For the calculations, MODTRAN is fed with the measured input parameters as presented in section 4. A selection of input data is listed in Table 5. Although the measured input data are temporally averaged (e.g., Sun photometer aerosol optical depth is averaged over 1 min), the calculations are performed for an instantaneous moment (see the times in Table 5).

[50] Before comparing the simulated surface shortwave irradiances to the measured irradiances, we will assess the uncertainties in the simulations. We assume that the model produces correct surface irradiances when fed with the correct solar insolation, surface reflectance, and atmospheric composition. Therefore the only sources of error in the modeled irradiances are the errors in model input parameters for the chosen MODTRAN4.1 setup. To estimate the magnitude of the errors in the calculated irradiances, we define two reference calculations on 19 June 2000: (1) at 12:30 UT (about 40 min after local solar noon) with θ_0 = 33.7°, (2) at 15:30 UT with θ_0 = 53.5°. In both reference calculations the input parameters are varied one-by-one with their measurement error or estimated error, while keeping the other parameters unchanged. The difference between the

Table 4. AVHRR-Derived 8 × 8 km^2 Surface Reflectances for an Area Centered Around De Bilt on 19 June 2000[a]

↑ 24 km ↓	R_1			R_2			A_s		
	0.12	0.11	0.11	0.29	0.26	0.22	0.20	0.19	0.17
	0.12	0.08	0.09	0.30	0.22	0.17	0.21	0.15	0.13
	0.10	0.09	0.08	0.20	0.19	0.19	0.16	0.14	0.14
	$\overline{R_1}$ = 0.10 ± 0.02			$\overline{R_2}$ = 0.23 ± 0.05			$\overline{A_s}$ = 0.16 ± 0.03		
	← 24 km →								

[a]The first two matrices contain channel 1 and channel 2 reflectances (R_1 and R_2), respectively. The third matrix contains the estimated shortwave broadband surface albedo (A_s) assuming Lambertian surface reflectance. The center value of each matrix corresponds to the pixel coordinates (52.110°N, 5.130°E) closest to the coordinates of De Bilt (52.100°N, 5.183°E). Area-averaged values and standard deviations are given below the matrices.

reference calculation and the perturbed reference calculation is a measure of the error in the calculated irradiance due to the error in the perturbed parameter.

5.2. Sensitivity Study

[51] In this section we will describe the error in each of the relevant input parameters of MODTRAN, and we will provide the resulting error in the calculated irradiances. In Tables 6 and 8 the MODTRAN reference and adjusted input parameter values are listed for the 12:30 UT and 15:30 UT runs for the case of 19 June 2000, respectively. The corresponding calculated irradiances are listed in Tables 7 and 9, respectively. For completeness, also the reflected irradiance at top of atmosphere (TOA), $E_{\uparrow,\mathrm{TOA}}$, and the absorbed irradiance in the atmosphere, $E_{abs} = (\mu_0 E_0 - E_{\uparrow,\mathrm{TOA}}) - E_{glo}(1 - A_s)$, are calculated for the selected days.

5.2.1. Sensitivity to Aerosol Optical Thickness Errors

[52] The calibrated Sun photometer provides the total optical thickness ($\tau = \tau_{Ray} + \tau_{gas} + \tau_{aer}$). Because the errors in the Rayleigh scattering optical thickness (τ_{Ray}) and the gaseous absorption optical thickness (τ_{gas}) are small compared to the errors in the aerosol optical thickness, the latter can be obtained from the Lambert-Beer law:

$$E(\lambda) = E_0(\lambda)\exp[-\tau M], \tag{11}$$

where M is the relative air mass. Using straightforward error calculus:

$$\Delta_{abs}\tau_{aer} = \left[(\Delta_{rel}M)^2 + \frac{(\Delta_{abs}\ln E_0)^2 + \left(\Delta_{abs}\ln\left(\frac{E_{dir}}{\mu_0}\right)\right)^2}{\left(\ln E_0 - \ln\left(\frac{E_{dir}}{\mu_0}\right)\right)^2}\right]^{\frac{1}{2}} \cdot \left\{1 + \frac{\tau_{Ray} + \tau_{gas}}{\tau_{aer}}\right\} \cdot \tau_{aer}, \tag{12}$$

where $\Delta_{rel}M$ is the relative error in the relative air mass, $\Delta_{abs}\ln E_0$ is the absolute error in the extraterrestrial irradiance as found from the SPUV calibration, and $\Delta_{abs}\ln(E_{dir}/\mu_0)$ is the absolute error in the measured DNSI. According to equation (12), the error in a single aerosol optical thickness value is the result of the combined error in relative air mass, the SPUV calibration, and the direct normal solar irradiance (DNSI) measurement. We estimate the relative error in the relative air mass to be 1% due to meteorological variations in temperature, pressure, or humidity relative to the well-mixed molecular standard atmosphere used to determine the relative air mass [*Young*, 1994]. We take a relative error of 2% in DNSI. The absolute error in the calibration factor, $\Delta_{abs}\ln E_0$, is the standard deviation of the mean calibration factor [*Henzing et al.*, 2001]. We thus find the aerosol optical thicknesses at 550 nm for the reference times: τ_{aer}(12:30 UT) = 0.20 ± 0.02 and τ_{aer}(15:30 UT) = 0.25 ± 0.02.

[53] In order to establish the sensitivity of the calculations to the error in τ_{aer}, the aerosol optical thickness is changed according to the above uncertainties. The fractional change at 550 nm is then applied to all other wavelengths. At 12:30 UT the error in aerosol optical thickness leads to an error in E_{dir}, E_{dif}, and E_{glo} of 11, 7, and 4 Wm^{-2}, respectively. At 15:30 UT the uncertainties in E_{dir}, E_{dif}, and E_{glo} are 9, 5, and 4 Wm^{-2}, respectively.

5.2.2. Sensitivity to Absorption Coefficient Errors

[54] The accuracy of k_{abs} is limited due to three major problems. One problem is the use of white light in the aethalometer to measure the absorption coefficient, which is essentially wavelength-dependent. Another problem is the loss of light, due to scattering particles on the filter, which is erroneously attributed to absorption. A third potential problem was discovered during our study, when we observed a decrease of aethalometer sensitivity when the total load on the filter increased, resulting in a nonlinear response.

[55] As a conservative estimate, we assume that k_{abs} is not better measured than within a factor of 2. As will be shown later, this limited accuracy does not preclude meaningful use of the aethalometer data in the model calculations. At 12:30 UT the best estimate of the aerosol absorption coefficient is $\overline{k_{abs}}$ = 6.9 × 10^{-6} m^{-1}, corresponding to a_{aer} = 0.89. Owing to the factor 2, the possible range of error for $\overline{k_{abs}}$ is [1.4 × 10^{-5} m^{-1}, 3.5 × 10^{-6} m^{-1}] and for a_{aer} [0.79, 0.94]. At 15:30 UT the best estimate is $\overline{k_{abs}}$ = 7.2 × 10^{-6} m^{-1} (a_{aer} = 0.89) with the range for $\overline{k_{abs}}$ [1.4 × 10^{-5} m^{-1}, 3.6 × 10^{-6} m^{-1}] and for a_{aer} [0.81, 0.94].

[56] In order to establish the sensitivity of the calculations to the error in the aethalometer measurements, the single scattering albedos at both ends of the range of error are used as model input. The total aerosol optical thickness is kept unchanged, so there are no consequences for E_{dir}. For both reference times the absolute effects on E_{dif}, and thus E_{glo}, are equal as can be seen from Tables 7 and 9. Increasing the aerosol absorption coefficient, E_{dif} and E_{glo} decrease by as much as 15 Wm^{-2}. With decreasing aerosol absorption the increase in E_{dif} and E_{glo} is 9 Wm^{-2}.

5.2.3. Sensitivity to Scattering Coefficient Errors

[57] The aerosol scattering coefficient is determined by the combined use of radiosonde, humidograph, and nephelometer measurements. As far as the radiosonde water vapor profile is concerned, it probably does not play a significant role in the overall error of the scattering coefficient. The

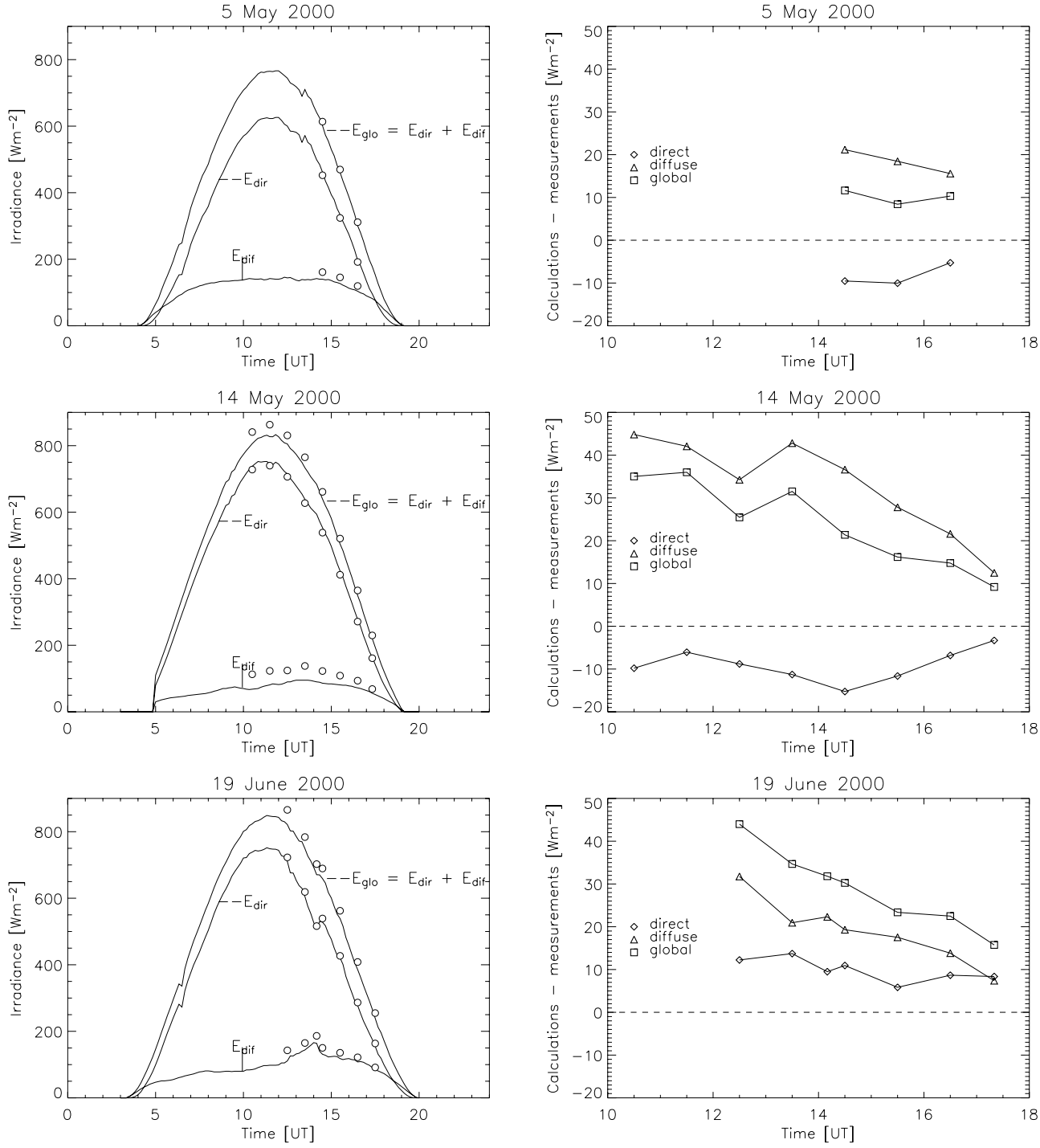

Figure 4. (left) Measurements of direct irradiance (E_{dir}), diffuse irradiance (E_{dif}), and the sum of direct and diffuse irradiance ($E_{dir} + E_{dif}$), for the 3 selected days, indicated by lines. Calculations of the same quantities are indicated by open circles. (right) The differences between measurements and calculations of direct, diffuse, and global (direct plus diffuse) irradiances for the 3 days.

determination of the dry scattering coefficient normally contributes most to the overall error. The drying in the nephelometer is accomplished by heating. Ammonium nitrate, which is the dominant aerosol for the Netherlands [*Ten Brink et al.*, 1996], is semivolatile and may (partly) evaporate upon heating. Such evaporation is indeed observed: on days with high RH decreases in signal of as high as 50% have been registered. On the days used in this study, surface RH is so low that drying is minimal and evaporative losses should be negligible. Probably the most important source of error for the scattering coefficient during our study is the translation of the ground-based measurement of the RH-dependence of the scattering coefficient to the boundary layer average scattering coefficient. Neglecting the RH dependence in the boundary layer, we find that $\overline{k_{sca}}$ (12:30 UT) is decreased from 5.4×10^{-5} m^{-1} to $5.1 \times$

Table 5. Selected Model Input Data[a]

	τ_{aer}								
Day, Time, UT	368 nm	500 nm	670 nm	780 nm	870 nm	α	a_{aer}	H_2O, kg m^{-2}	H_{bl}, m
5 May, 14:30	0.6155	0.3634	0.1828	0.1328	0.1352	1.87	0.925	16.69	1850
5 May, 15:30	0.6268	0.3838	0.2078	0.1497	0.1426	1.79	0.923	16.97	1880
5 May, 16:30	0.6338	0.3986	0.2267	0.1633	0.1494	1.72	0.931	17.25	1880
14 May, 10:30	0.3192	0.1624	0.0466	0.0344	0.0579	2.23	0.885	11.37	1100
14 May, 11:30	0.3602	0.1953	0.0613	0.0464	0.0668	2.17	0.876	11.56	1200
14 May, 12:30	0.4034	0.2235	0.0796	0.0596	0.0794	2.09	0.827	11.86	1420
14 May, 13:30	0.4398	0.2540	0.1049	0.0779	0.1020	1.90	0.875	12.17	1680
14 May, 14:30	0.3919	0.2269	0.0974	0.0703	0.0976	1.83	0.871	12.47	1700
14 May, 15:30	0.3838	0.2229	0.1042	0.0739	0.0970	1.80	0.862	12.78	1690
14 May, 16:30	0.3677	0.2183	0.1114	0.0794	0.0935	1.76	0.886	13.09	1670
14 May, 17:30	0.3224	0.1892	0.1066	0.0758	0.0764	1.74	0.850	13.28	1640
19 June, 12:30	0.4793	0.2481	0.0925	0.0699	0.0872	2.22	0.885	18.95	1500
19 June, 13:30	0.6364	0.3508	0.1595	0.1194	0.1268	2.04	0.873	20.40	1800
19 June, 14:10	0.8213	0.4700	0.2353	0.1744	0.1707	1.94	0.881	21.33	2000
19 June, 14:30	0.5768	0.3182	0.1492	0.1141	0.1217	1.98	0.881	21.85	2000
19 June, 15:30	0.5385	0.3021	0.1499	0.1136	0.1181	1.91	0.893	23.29	2000
19 June, 16:30	0.5607	0.3258	0.1755	0.1325	0.1294	1.81	0.900	24.74	2000
19 June, 17:30	0.5008	0.3005	0.1738	0.1314	0.1245	1.70	0.889	26.04	2000

[a]The data are obtained as described in section 4.3.

10^{-5} m^{-1}, so a_{aer} decreases from 0.89 to 0.88. A similar decrease in a_{aer} occurs for the 15:30 UT case.

[58] In order to establish the sensitivity of the irradiance calculations to the error in the boundary layer average aerosol scattering coefficients, the single scattering albedos corresponding to completely dry atmospheres (a_{aer} = 0.88) at the reference times are used as model input. The results are in Tables 7 and 9. Again E_{dir} is not affected. For both reference times the absolute effects on E_{dif} (E_{glo}) are equal. For the dry atmosphere, E_{dif} and E_{glo} decrease by a modest 1 Wm^{-2}.

5.2.4. Sensitivity to Asymmetry Parameter Errors

[59] Aerosol size distribution measurements are used to obtain the asymmetry parameter using Mie theory. Unfortunately, the size distribution is not measured on 5 and 14 May 2000. On the basis of a great many size distribution measurements at Petten in the past, it can be concluded that a size of r_g = 0.055 μm, as measured on 19 June 2000, is quite small. Therefore we calculate the asymmetry parameter also for a size distribution with larger particles, namely, with r_g = 0.1 μm. However, the Angström parameter that follows from the Sun photometer measurements (Figure 3, right panels), suggests that the aerosol size distribution consists of smaller particles. For 19 June 2000, 12:30 UT (15:30 UT), we need to lower the median radius to r_g = 0.037 μm (r_g = 0.048 μm) in order to meet the Sun photometer spectral dependence, which has an Angström parameter of 2.2 (1.9). In Table 3 the asymmetry parameters corresponding to the measured size distribution and for the small and large particles are given for the selected wavelengths. It can be seen that g is larger for larger particles as expected.

[60] The asymmetry parameters of the smaller and larger particles are used to establish the sensitivity of the irradiance calculations for the error in the asymmetry parameter. As is shown in Tables 7 and 9, E_{dir} is unaffected. E_{dif} and E_{glo} are increased in the perturbed calculation, because the larger particles scatter more in the forward direction,. At 12:30 UT (15:30 UT) E_{dif} and E_{glo} are increased with 3 (5) Wm^{-2}. The smaller particles scatter more uniformly in all directions, so that E_{dif} and E_{glo} are decreased in the perturbed calculation. At 12:30 UT (15:30 UT) E_{dif} and E_{glo} are decreased with 4 (2) Wm^{-2}.

5.2.5. Sensitivity to Water Vapor Column Errors

[61] A reasonable estimate of the error in the atmospheric water vapor column is 10%. At 12:30 UT we find H_2O = 19.0 ± 1.9 kg m^{-2}. At 15:30 UT, H_2O = 23.3 ± 2.3 kg m^{-2}. This error in absorption by water vapor leads to an error in both E_{dir} and E_{glo} of 4 and 3 Wm^{-2} at 12:30 UT and

Table 6. MODTRAN Input Values Used in the 19 June 2000, 12:30 UT, Reference Run Are Given in Column 3 (“Reference Value”)[a]

Input Parameter	Symbol	Reference Value	Applied Change	Explanation	Adjusted Value	Consequence
Aerosol optical thickness (550 nm)	τ_{aer}	0.20	+0.02	measurement error	0.22	
			−0.02		0.18	
Asymmetry parameter (501 nm)	g	0.638	see text	larger particles	0.694	
				smaller particles	0.567	
Aerosol absorption coefficient	$\overline{k_{abs}}$	6.9 × 10^{-6} m^{-1}	×2	measurement error	13.9 × 10^{-6} m^{-1}	a_{aer} = 0.79
			× $^1/_2$		3.5 × 10^{-6} m^{-1}	a_{aer} = 0.94
Aerosol scattering coefficient	$\overline{k_{sca}}$	5.4 × 10^{-5} m^{-1}	−0.3	assumed dry air (aerosol scattering insensitive to RH)	5.1 × 10^{-5} m^{-1}	a_{aer} = 0.88
Surface albedo	A_s	0.15	+0.03	standard deviation	0.18	
			−0.03		0.12	
Boundary layer height	H_{bl}	1500 m	×2	experiment	3000 m	
Water vapor column	H_2O (g)	18.95 kg m^{-2}	+10%	interpolation error	20.85 kg m^{-2}	
			−10%		17.05 kg m^{-2}	

[a]Values used in the sensitivity study are given in column 6 (“adjusted value”). Reference values and applied changes of the input parameters are described in the corresponding subsections of section 5.

Table 7. MODTRAN Results for 19 June 2000, 12:30 UT[a]

MODTRAN Run		E_{dir}, W m^{-2}	E_{dif}, W m^{-2}	$E_{dir}+E_{dif}$, W m^{-2}	$E_{\uparrow,\mathrm{TOA}}$, W m^{-2}	E_{abs}, W m^{-2}
Irradiance of reference run		723	142	865	170	232
No aerosol		+122	−84	+38	−4	−28
Aerosol optical thickness	increased	−11	+7	−4	+0	+2
	decreased	+11	−7	+4	−0	−3
Asymmetry parameter	larger particles	0	+3	+3	−2	−1
	smaller particles	0	−4	−4	+3	+1
Aerosol absorption coefficient	increased	0	−15	−15	−6	+19
	decreased	0	+9	+9	+4	−13
Aerosol scattering coefficient	dry air	0	−1	−1	−0	+0
Surface albedo	increased	0	+2	+2	+21	−23
	decreased	0	−2	−2	−21	+22
Boundary layer height	increased	0	+0	+0	−1	−0
Water vapor column	increased	−4	−0	−4	−1	+4
	decreased	+4	+0	+4	+1	−5

[a]Incident irradiance at TOA is $\mu_0 E_0 = 1138$ W m^{-2}, $\theta_0 = 33.7°$. Differences (adjusted calculation minus reference calculation) are in W m^{-2}. The input (reference and adjusted) parameters are given in Table 6.

15:30 UT, respectively (see Tables 7 and 9). The effect on E_{dif} is less than 1 Wm^{-2} at both reference times.

5.2.6. Sensitivity to Surface Albedo Errors

[62] The shortwave broadband surface albedo used in the simulations is obtained using AVHRR channel 1 and 2 reflectances for the single 8 × 8 km^2 pixel containing the measuring site, as described in section 4.2.7. A second estimate of the albedo is obtained by averaging the broadband reflectances of the nine AVHRR 8 × 8 km^2 pixels surrounding the measuring site. Doing so, we find $A_s = 0.16 \pm 0.03$.

[63] The standard deviation 0.03 is used to investigate the sensitivity of the calculated irradiances to the assumed broadband surface albedo. As can be seen from Tables 7 and 9, the effect of the exercise $A_s \pm 0.03$ is strongest for the reflected irradiance at the top of the atmosphere: at 12:30 UT $E_{\uparrow,\mathrm{TOA}}$ increases by 21 Wm^{-2} for the 0.03 increase of A_s, whereas at 15:30 UT $E_{\uparrow,\mathrm{TOA}}$ increases by 13 Wm^{-2} for the 0.03 increase of A_s. The effect on the surface irradiances is less pronounced: the increase of A_s, which increases multiple reflections between the surface and the atmosphere, increases $E_{\downarrow}$ by 2 W m^{-2} for both reference times.

5.3. Total Error in the Calculated Irradiances

[64] We express the error in the calculated irradiances due to the error in model input parameter x_i as:

$$\Delta E_{rad,i} = \left(\frac{\partial E_{rad}}{\partial x_i}\right)\Delta x_i. \tag{13}$$

Here *rad* stands for *dir*, *dif*, or *glo* and $(\partial E_{rad}/\partial \mathrm{x}_i)$ represents the sensitivity, defined as the change in the computed E_{rad} for a unit change in input parameter x_i, keeping all other parameters constant. Assuming that all input parameters are independent, we estimate the overall error in the calculated irradiances due to uncertainties in the input parameters as:

$$\Delta_{calc} E_{rad} = \sqrt{\sum_i \left(\Delta E_{rad,i}\right)^2} \tag{14}$$

(Wm^{-2}). The errors in the calculated irradiances are listed together with the irradiance measurement errors in Table 2.

6. Comparison Between Modeled and Measured Downward Shortwave Clear-Sky Irradiances

6.1. Comparison Strategy

[65] We define the difference between modeled and measured irradiances as:

$$DE_{rad} = E_{rad,calc} - E_{rad,meas}. \tag{15}$$

The error in DE_{rad} is then given by

$$\Delta DE_{rad} = \left[\left(\Delta_{calc} E_{rad}\right)^2 + \left(\Delta_{meas} E_{rad}\right)^2\right]^{1/2} \tag{16}$$

since the errors in measured and calculated irradiances are uncorrelated. Using equation (16) and the values of

Table 8. MODTRAN Input Values Used in the 19 June 2000, 15:30 UT, Reference Run Are Given in Column 3 (“Reference Value”)[a]

Input Parameter	Symbol	Reference Value	Applied Change	Explanation	Adjusted Value	Consequence
Aerosol optical thickness (550 nm)	τ_{aer}	0.25	+0.02	measurement error	0.27	
			−0.02		0.23	
Asymmetry parameter (501 nm)	g	0.638	see text	larger particles	0.694	
				smaller particles	0.567	
Aerosol absorption coefficient	$\overline{k_{abs}}$	7.2 × 10^{-6} m^{-1}	×2	measurement error	14.3 × 10^{-6} m^{-1}	$a_{aer} = 0.81$
			× $^1/_2$		3.6 × 10^{-6} m^{-1}	$a_{aer} = 0.94$
Aerosol scattering coefficient	$\overline{k_{sca}}$	6.0 × 10^{-5} m^{-1}	−0.4	assumed dry air (aerosol scattering insensitive to RH)	5.6 × 10^{-5} m^{-1}	$a_{aer} = 0.88$
Surface albedo	A_s	0.15	+0.03	standard deviation	0.18	
			−0.03		0.12	
Boundary layer height	H_{bl}	2000 m	×2	experiment	4000 m	
Water vapor column	H_2O (g)	23.3 kg m^{-2}	+10%	interpolation error	25.6 kg m^{-2}	
			−10%		21.0 kg m^{-2}	

[a]Values used in the sensitivity study are given in column 6 (“adjusted value”). Reference values and applied changes of the input parameters are described in the corresponding subsections of section 5.

Table 9. MODTRAN Results for 19 June 2000, 15:30 UT[a]

MODTRAN Run		E_{dir}, W m^{-2}	E_{dif}, W m^{-2}	$E_{dir}+E_{dif}$, W m^{-2}	$E_{\uparrow,\mathrm{TOA}}$, W m^{-2}	E_{abs}, W m^{-2}
Irradiance of reference run		427	136	562	139	196
No aerosol		+134	−84	+49	−13	−29
Aerosol optical thickness	increased	−8	+5	−4	+1	+2
	decreased	+9	−5	+4	−1	−2
Asymmetry parameter	larger particles	0	+5	+5	−3	−0
	smaller particles	0	−5	−5	+3	+0
Aerosol absorption coefficient	increased	0	−15	−15	−7	+20
	decreased	0	+9	+9	+5	−12
Aerosol scattering coefficient	dry air	0	−1	−1	−0	+1
Surface albedo	increased	0	+2	+2	+13	−15
	decreased	0	−2	−2	−13	+15
Boundary layer height	increased	0	−0	−0	+0	+0
Water vapor column	increased	−3	−0	−3	−1	+3
	decreased	+3	+0	+3	+1	−4

[a]Incident irradiance at TOA is $\mu_0 E_0$ = 813 W m^{-2}, θ_0 = 53.5°. Differences (adjusted calculation minus reference calculation) are in W m^{-2}. The input (reference and adjusted) parameters are given in Table 8.

$\Delta_{calc}E_{rad}$, given in section 5.3, and the values of $\Delta_{meas}E_{rad}$ given in Table 2, we find the estimated errors ΔDE_{rad} for the reference calculated irradiances listed in Table 2.

6.2. Direct Irradiances

[66] For 5 May and 14 May 2000 the calculated direct irradiances are always smaller than the measured irradiances with a typical difference of 5–15 Wm^{-2} (see Figure 4, right panels). On 19 June 2000, however, the situation is reversed but the differences are of the same order of magnitude. Even when we assume that the smallest error estimate of ΔDE_{dir}, is applicable, namely, 14 Wm^{-2}, we find all individual differences, DE_{dir}, to be smaller than, or very close to ΔDE_{dir}. Therefore we conclude that modeled and measured surface downward direct irradiances agree within the estimated uncertainty.

6.3. Diffuse Irradiances

[67] For the diffuse irradiance there is less good agreement between the modeled and measured irradiances. For all cases the calculated diffuse irradiances are higher than the measured irradiances, DE_{dif} being between 7 and 44 Wm^{-2}. The calculations and measurements tend to converge toward the end of the day, particularly on 14 May and 19 June. Despite the large error in the difference, the maximum ΔDE_{dif} being 18 Wm^{-2}, only 5 out of the 18 comparisons agree within the estimated uncertainty.

6.4. Global Irradiances

[68] As was the case for the diffuse irradiance, all calculated values of the global irradiance are higher than the measured values, DE_{glo} being between 8 and 44 Wm^{-2}. The trends that are seen in DE_{dif} are also present in DE_{glo}. The calculated values of E_{glo} generally agree best with the measurements for low Sun elevation. Despite the large error in the difference, the maximum being 21 Wm^{-2}, only 8 out of the 18 comparisons agree within the estimate uncertainty.

[69] In conclusion, we find that calculated and measured direct irradiances at the ground agree within the combined error estimate. However, for the diffuse and global irradiances, we find that the calculated irradiances overestimate the measured irradiances. For a big majority of cases, the magnitude of the overestimation cannot be explained by pyranometer measurement errors, or by the error in the used model input parameters, or by a combination of both. Moreover, the overestimation seems to be dependent on the time on the day; the magnitude of DE_{dif} increases with increasing μ_0 for all three cases (Figure 5, top). In Figure 5 (bottom) the magnitude of DE_{dif} relative to the incoming irradiance at TOA ($\mu_0 E_0$) is shown. The relative model-measurement difference shows no significant correlation with μ_0, differences roughly amount 1–4% of TOA irradiance. This is in agreement with the results that we derive from *Halthore and Schwartz* [2000, Table 1] (43 cases), who also find values of 1–4%. In the next section we will discuss sources of errors that may lead to the systematic deviations from zero in DE_{dif}.

6.5. Discussion of Possible Sources of the Disagreement Between Calculated and Measured Irradiances

[70] Above we estimated the error in the difference between modeled and measured irradiances by including the uncertainties of the measurements that served as input for the model calculations. We saw that calculated and measured diffuse and global irradiances did not agree within the error estimate. In this section we will discuss some other uncertainties that can lead to a disagreement between calculated and measured irradiances.

6.5.1. Spectral Aerosol Optical Thickness

[71] In the model calculations, the aerosol optical thicknesses at wavelengths longer than 870 nm are obtained by extrapolation using the Angström relation. However, from measurements in Petten we know that on 19 June 2000 (but also on other days with synoptic conditions similar to those in our study) the size distribution is bimodal. The fact that τ_{aer}(870 nm) is equal to or larger than τ_{aer}(780 nm) for the 3 selected days confirms this. To study the effect of higher optical thickness of the aerosols at longer wavelengths, we recalculate the irradiances at the two reference times increasing the aerosol optical thickness to τ_{aer}(870) at 1000 nm (case I) and 1500 nm (case II), keeping the aerosol optical thickness constant in-between and using the Angström relation for longer wavelengths. Increasing the aerosol optical thickness reduces the direct irradiance by 4 (10) Wm^{-2} for case I (case II) at both reference times. The corresponding increase in diffuse irradiances is 3 (6) Wm^{-2} at both reference times. Using these irradiance

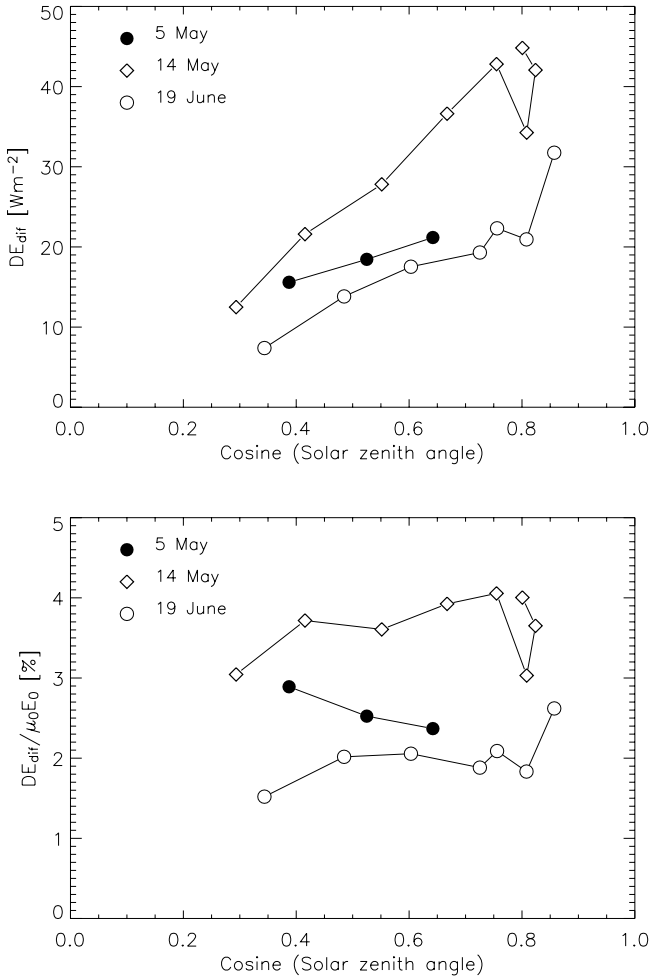

Figure 5. (top) The difference between calculated and measured diffuse irradiances plotted as a function of the cosine of the solar zenith angle (μ_0). Individual comparisons on a single day (diamonds) are connected by a thin black line. (bottom) Same, but relative to the top-of-atmosphere incoming irradiance, $\mu_0 E_0$.

values for case I (case II), 3 (10) out of 18 (18) comparisons of the direct irradiance do not agree within the error estimate (originally model and measurements agreed). For diffuse irradiance the situation also gets worse, only 4 (2) out of 18 (18) comparisons agree within the error estimate (originally we found agreement for 5 out of 18 comparisons). In view of this large effect, measurements of τ_{aer} at longer wavelengths (e.g., at 1000, 1600, and 2200 nm) are desirable in later studies.

6.5.2. Surface Albedo

[72] In our model we use a spectrally flat albedo. However, for vegetation the surface albedo in the visible spectral region is generally smaller than at longer wavelengths [*Bowker et al.*, 1985]. The spectrally independent surface albedo is thus too reflective in the visible and too little reflective in the near infrared. Since scattering by the atmosphere is stronger in the visible spectral region than in the near infrared, the use of the broadband albedo will consequently lead to a modeled E_{dif} that is too high. Indeed, using the reflectances derived from AVHRR channels 1 (8%) and 2 (22%) for the visible region (VIS, $\lambda < 700$ nm) and the near infrared region (NIR, $\lambda > 700$) as was done in section 4.3.7, we find that due to the assumption of a spectrally flat albedo of 0.15, E_{dif} is overestimated by 4 and 2 Wm^{-2} for 19 June 12:30 UT and 15:30 UT, respectively.

[73] Furthermore, in our model we use a constant albedo over the day. In reality, however, the surface albedo depends on the solar zenith angle. To obtain a representative solar zenith angle dependence of the surface albedo of our site, we use data from upward and downward looking pyranometers over pasture in Cabauw (less than 20 km SW of the measuring site) at 19 June 2000. Although this surface albedo increases with increasing solar zenith angle by almost 50% over the range of zenith angles in this study, its effect on the downward diffuse irradiance and on DE_{dif} is only 1–2 Wm^{-2}, due to the partly canceling effect of increasing surface albedo and decreasing incoming irradiance with increasing solar zenith angle. We therefore conclude that the large differences between modeled and measured surface downward irradiances and, more specific, the trend in the differences cannot be explained by uncertainties in the surface albedo.

6.5.3. Zero Offset of Pyranometer Measurements

[74] As explained in section 3.2, we chose not to correct the pyranometer measurements for thermal offset errors. In view of the differences between measured and modeled irradiances it is nevertheless useful to give a rough estimate of the error involved. Nighttime offsets in Cabauw typically vary between +1 and −6 Wm^{-2}, where the latter value occurs during clear-sky nights such as the ones prior to and after the measurement days used in this study. However, it is well-known that during clear-sky conditions daytime values of the thermal offset are larger than nighttime values [*Cess et al.*, 2000; *Dutton et al.*, 2001]. However, these works suggest that the daytime offset does not exceed the nighttime offset by a factor of 2. This implies that a liberal estimate of the daytime offset for the cases described here is 12 Wm^{-2} and probably smaller. In view of the values of DE_{dif} and DE_{glo}, the conclusion is justified that the pyranometer zero-offset alone cannot explain the differences between modeled and measured irradiances. It should, however, be mentioned that this offset does reduce the discrepancy, but the precise reduction is unknown. Since model-measurement differences seem to be a fixed fraction of the incoming irradiance at TOA (Figure 5, bottom), it is not very likely that the pyranometer zero offset is causing an important fraction of the discrepancy, as it would have led to a systematic model-measurement difference independent of solar insolation.

6.5.4. Vertical Aerosol Distribution

[75] In our study, we assume that all aerosols are confined to a well-mixed boundary layer, which is an idealized representation of the reality. This assumption is almost harmless with respect to surface downward irradiances, if optical properties of aerosols above the boundary layer do not deviate from boundary layer aerosol, see the double boundary layer height experiments in Tables 6–9. However, if free-tropospheric and stratospheric aerosols, with different asymmetry parameters and/or single scattering albedos, are responsible for a significant fraction of the aerosol optical thickness, then the calculated diffuse irradiances are erroneous. To estimate this effect, we use the MODTRAN built-

in aerosol climatology [*Shettle and Fenn*, 1979] with free tropospheric aerosol and stratospheric aerosol. The aerosol optical thickness as obtained from the Sun photometer is distributed over the boundary layer (τ_{aer}(12:30) = 0.12 and τ_{aer}(15:30) = 0.15 at 500 nm), free troposphere (τ_{aer} = 0.11 and τ_{aer} = 0.14), and stratosphere (τ_{aer} = 0.01). The result is that, compared to the standard runs for 19 June 12:30 and 15:30 UT, E_{dif} increases by 9 and 7 Wm^{-2}, respectively. Thus the difference with the measurements increases. Larger single scattering albedos and increased forward scattering by larger particles, included in the aerosol climatology, cause the increase. To obtain agreement between calculated and measured E_{dif}, the single scattering albedo and asymmetry parameter of the aerosol above the boundary layer should be decreased to values far beyond the smallest values accepted in the sensitivity calculations. We believe that free tropospheric aerosol (aerosol optical thickness of stratospheric aerosol is too small to be of any importance) with those characteristics is unrealistic.

7. Discussion of a Possible Agreement Between Modeled and Measured Diffuse Irradiances

[76] In an attempt to determine when we do find agreement between modeled and measured diffuse irradiances, we varied the single scattering albedo and the median radius of the lognormal distribution beyond uncertainty estimates. The results of these model calculations are shown in Figure 6.

[77] In Figure 6 (top) the largest single scattering albedos cause the largest modeled-measured diffuse irradiance differences, DE_{dif}. Decreasing the single scattering albedo to 0.70 and 0.79, we find closure for 19 June 12:30 and 15:30 UT, respectively. Although both single scattering albedos are outside the measurement uncertainty limits, they are not completely improbable. However, for 14 May 2000, the model-measurement differences are much larger, whereas τ_{aer} is much lower (Figure 3, left panels). Consequently the single scattering albedo has to be lowered more rigorously to 0.56 and 0.61 for 14 May 12:30 and 15:30, respectively. Such low single scattering albedos do not only fall outside the measurement uncertainty limits, they are very low even for heavy industrialized areas or metropolitan city centers.

[78] In Figure 6 (bottom) the largest median radii, corresponding to common size distributions in the Netherlands, cause the largest model-measurement differences. The smaller the particle median radius is chosen, the smaller DE_{dif} becomes. For 19 June 2000, agreement is obtained for particles as small as 0.003 and 0.015 μm for 12:30 and 15:30 UT, respectively. For 14 May 2000, it is not possible to find agreement by reducing the aerosol particle sizes.

[79] In the following, we will make first order estimates of three corrections that reduce DE_{dif}. We discussed in section 3.1 that the pyrheliometer is measuring forward scattered light as diffuse irradiance. The shaded pyranometer is missing exactly this diffuse irradiance. We estimated the missing diffuse irradiance being 1.4 and 1.6 Wm^{-2} for 19 June 12:30 and 15:30, respectively. Furthermore, we applied a spectrally flat albedo in our calculations. In section 6.5.2 we showed that this leads to an overestimate of the modeled diffuse irradiance. We estimated the amount to be 4 and 2 Wm^{-2} for 19 June 12:30 and 15:30,

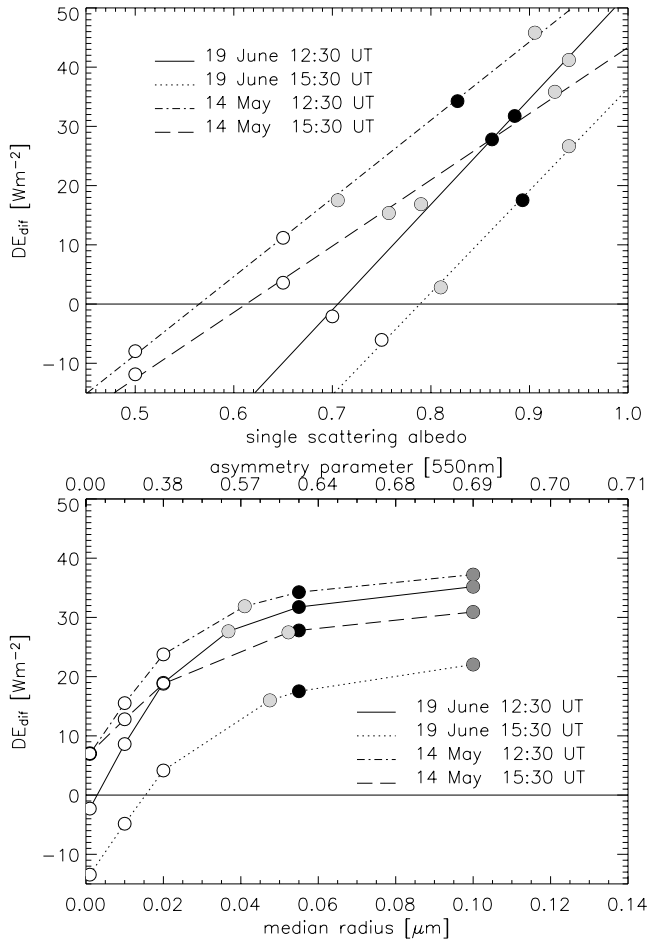

Figure 6. Differences between modeled and measured diffuse irradiance, DE_{dif}, as a function of single scattering albedo, a_{aer} (top) and median radius or asymmetry parameter (bottom). In each plot, DE_{dif} is given for two low aerosol optical thickness cases (14 May, 2000, 12:30 UT, θ_0 = 36° and 15:30 UT, θ_0 = 57°) and two high aerosol optical thickness cases (19 June, 2000, 12:30 UT, θ_0 = 34° and 15:30 UT, θ_0 = 54°). (top) Black solid circles indicate the values used in the standard calculations of Figure 4. Grey solid circles correspond to calculations with the decreased aerosol absorption (high a_{aer}) and the increased aerosol absorption (high a_{aer}) of Tables 6–9. Agreement, i.e., DE_{dif} = 0, is obtained when a_{aer} = 0.70 and a_{aer} = 0.79 for 19 June 12:30 and 15:30 UT, respectively; for 14 May 12:30 and 15:30 UT, agreement is obtained when a_{aer} = 0.56 and a_{aer} = 0.61, respectively. (bottom) Solid circles indicate the values used in the standard calculations of Figure 4; light grey circles indicate the median radius for which the Mie calculated Angström parameter equals the Sun photometer Angström parameter; dark grey circles correspond to climatological large particles. Agreement is obtained for r_g = 0.003 μm and r_g = 0.015 μm for 19 June 12:30 and 15:30 UT, respectively. For the case of 14 May (low aerosol optical thickness), no agreement can be obtained by reducing the aerosol particle size.

respectively. To obtain the asymmetry parameter, we applied Mie calculations for a lognormal distribution with the median radius and standard deviation as obtained from microphysical measurements in Petten. As an alternative, we can use the Angström parameter as measured with the Sun photometer to obtain the median radius of the lognormal size distribution. This results in a smaller asymmetry parameter and thus less forward scattering. For 19 June 12:30 and 15:30 we find a reduction of the modeled diffuse irradiance of 4 and 2 Wm^{-2}, respectively. Summing the above values, that all work in the same direction, we find that the differences between modeled and measured diffuse irradiances are reduced by 9.4 and 5.6 Wm^{-2} for 19 June 12:30 and 15:30 UT, respectively. We find $DE_{dif} = 22 \pm 18$ Wm^{-2} and $DE_{dif} = 12 \pm 18$ Wm^{-2} for 19 June 12:30 and 15:30 UT, respectively. For 15:30 UT we now find agreement. For 12:30 UT we need a realistic pyranometer zero offset of 4 Wm^{-2} to bring calculations and measurements into agreement. It is thus possible to find agreement between calculated and measured surface diffuse irradiances for the two reference calculations. Applying the largest correction (9.4 Wm^{-2}) 11 out of 18 comparisons agree without having to apply a correction for pyranometer zero offset. If, moreover, the maximum zero offset estimate of 12 Wm^{-2}, given in section 6.5.3, is used for correction, we find that 17 out of 18 comparisons agree within the uncertainty estimates. For 14 May 10:30 UT the needed zero offset is 13.4 Wm^{-2} and thus exceeds the maximal zero offset. Moreover, it should be mentioned that, after applying the largest correction to all calculations, calculated values remain always larger than measured irradiances, except for 19 June 17:30 UT.

[80] Despite the partly obtained closure, there is still the fact that modeled diffuse irradiances exceed measured diffuse irradiances while direct irradiances are predicted correctly. This may indicate an erroneous aerosol scattering phase function or missing atmospheric absorption. A readily identifiable gas responsible for anomalous continuum absorption, as suggested by, for example, *Kato et al.* [1997] and *Halthore and Schwartz* [2000], is absent. It is unlikely that missing absorption is the result of a gaseous line absorber, because it is very unlikely that such a line absorber would not have been recognized until now [*Solomon et al.*, 1998; *Mlawer et al.*, 2000]. We believe that the residual optical thickness that is obtained after subtracting molecular scattering and absorption from total extinction as measured with the Sun photometer is caused by particles. We know that a smaller single scattering albedo and asymmetery parameter, associated with smaller particles, will reduce the calculated downward diffuse solar irradiance for a given aerosol optical thickness. To explain the model-measurement discrepancy, a_{aer} and g have to be changed beyond estimated uncertainty limits. However, for small particles ($r_g < 0.1$ μm), the single scattering albedo and asymmetry parameter are very sensitive to both the median size r_g and the standard deviation σ. Both a_{aer} and g decrease drastically as r_g and σ decrease [e.g., *Wendisch et al.*, 2002; *Fu et al.*, 1998]. Therefore it is possible that our uncertainty limits have been set too rigorously and that a narrower size distribution shifted toward smaller particles exists. The median radius of the lognormal distribution used in our calculations is possibly too large (compare the Sun photometer Angström parameter). We can expect aerosols to be smaller than 0.1 μm for the low relative humidities that were present throughout the whole atmosphere at our comparison days (RH < 70%). The width of the lognormal distribution is therefore possibly taken too large. So, if these small particles do exist and are responsible for part of the extinction measured with the Sun photometer, why do we not observe the correspondingly high absorption coefficient? We suggest two possibilities why these small particles are neglected in the aethalometer measurement. First, ultrafine particles with radii smaller than 0.025 μm are transported primarily by Brownian diffusion. They are therefore efficiently transported toward the surface where they are absorbed [*Wesely*, 1989; *Seinfeld and Pandis*, 1998]. Thus ultrafine particles present everywhere in the boundary layer (and above) may contribute to the aerosol extinction as observed with Sun photometry, but they may not be as numerous near the surface and may not contribute to the measured aerosol absorption coefficient. Second, the aethalometer is designed to obtain absorbing carbonaceous aerosol concentrations. Therefore the used aethalometer filter (Tissuquartz, Pallflex company), with aerosol retention close to 100% for particles larger than 0.3 μm, should be suitable for this purpose. However, the retention for smaller aerosol particles, that hypothetically absorb light, is not very well known and certainly less than 100%. So, if these small particles are indeed undetected by the aethalometer, then the relevant question is whether they are numerous enough to be of any importance in terms of aerosol optical thickness. This remains to be investigated as future work.

8. Conclusions

[81] The analysis for 18 cases of model calculations and measurements of clear-sky surface irradiances revealed no discernable difference between model and measurement for the direct irradiance, but several significant differences for the diffuse (and, consequently, global) irradiance. The differences between modeled and measured direct irradiance vary between −15 Wm^{-2} and +14 Wm^{-2}, with an average of −2 Wm^{-2}. Since the uncertainty in the difference varies between 14 and 16 Wm^{-2}, there is no evidence for a disagreement between model and measurement. For the diffuse irradiance, however, the measurement is always overestimated by the model. The overestimation varies from 7 to 44 Wm^{-2}, with an average of 25 Wm^{-2}. Since the uncertainty in the difference is estimated to be 18 Wm^{-2}, a majority of the cases (to be precise: 13 out of 18) reveals a significant overestimation of the measurements by the model.

[82] Several instrument imperfections and model assumptions are likely to have caused biases that, in particular in combination, contribute to the discrepancy mentioned. Examples are: the pyranometer zero-offset, the portion of diffuse radiation that is not measured by the shaded pyranometer, the use of a wavelength-independent surface albedo, and the use of Mie calculations instead of Sun photometer measurements for the calculation of the aerosol asymmetry parameter. Although it is difficult to assess the precise magnitude of these biases, we estimate the cumulative effect between 5 and 21 Wm^{-2}, where the largest variation comes from the uncertainty in the zero-offset. In

the worst case (21 Wm^{-2}), only one of the 18 cases reveals a significant overestimation of the measurement by the model. It should be noted, however, that this situation is based on the crude assumption that the daytime pyranometer zero-offset amounts to twice the typical nighttime value. If we relax this assumption, to values that are probably more realistic, then several cases point to a persistent and significant positive model-measurement difference for the diffuse irradiance. This difference amounts to typically 1–4% of the top-of-atmosphere irradiance, and does not depend on the solar zenith angle.

[83] In order to shed light on the reason for the discrepancy for diffuse irradiance, we performed a model sensitivity analysis for the aerosol single scattering albedo and the mean radius, which is related to the asymmetry parameter (Figure 6). The analysis learned that closure can be obtained for smaller single scattering albedo or mean radius. Although the values have to be adjusted beyond the measurement uncertainty, the analysis seems to point to an explanation in terms of small aerosol particles. In particular, a size distribution that includes a branch of very small particles may very well remove the discrepancy for the diffuse irradiance. It is conceivable that these particles have not been detected by the instrument for measuring aerosol absorption, because they are simply too small, but also because they may not be so dominantly present near the surface, where dry deposition leads to removal of these particles. In both cases, too little aerosol absorption may have been measured, and too much forward scattering may have been assumed, leading to an overestimation of modeled diffuse irradiance.

[84] A future experiment may focus on the suggested presence of ultrafine absorbing aerosols, and on the question if these particles exist in a sufficient concentration to significantly reduce model calculations of the surface diffuse irradiance. Needless to say, such efforts are not very useful if other measurement uncertainties are not reduced. Two aspects that need special attention are the pyranometer zero-offset and the Sun photometer calibration. Meanwhile, KNMI is in the process of updating its radiation measurements to the standards of the Baseline Surface Radiation Network (BSRN [*Ohmura et al.*, 1998]) and the operational Sun photometer has been calibrated at the High Altitude Research Station Jungfraujoch [*Knap and Los*, 2004].

[85] **Acknowledgments.** This work was supported by the Dutch National Research Programme on Global Air Pollution and Climate Change project 951272. We would like to thank G. Anderson and A. Berk (Air Force Research Laboratory, Hanscom, Massachusetts) for kindly providing the MODTRAN4 model. Support from E. Shettle and A. Berk in using the model regarding aerosols is gratefully acknowledged. We thank three anonymous reviewers for their comments and suggestions that considerably improved the manuscript.

References

Agbu, P. M., and M. E. James (1994), The NOAA/NASA pathfinder AVHRR land data set user's manual, Goddard Distrib. Active Arch. Cent., NASA Goddard Space Flight Cent., Greenbelt, Md.

Anderson, G. P., S. A. Clough, F. X. Kneizys, J. H. Chetwynd, and E. P. Shettle (1986), AFGL atmospheric constituent profiles (0–20 km.), *Rep. AFGL-TR-86-0110*, U.S. Air Force, Hanscom Air Force Base, Mass.

Ansmann, A., U. Wandinger, A. Wiedensohler, and U. Leiterer (2002), Linderberg Aerosol Characterization Experiment 1998 (LACE 98): Overview, *J. Geophys. Res.*, *107*(D21), 8129, doi:10.1029/2000JD000233.

Apituley, A., E. P. Visser, J. B. Bergwerff, J. M. de Winter, H. de Backer, and M. A. F. Allaart (1997), RIVM tropospheric ozone lidar routine measurements, validation, and analyses, in *Advances in Atmospheric Remote Sensing*, edited by A. Ansmann et al., pp. 375–378, Springer-Verlag, New York.

Arking, A. (1996), Absorption of solar energy in the atmosphere: Discrepancy between model and observations, *Science*, *273*, 779–782.

Arking, A. (1999a), Bringing climate models into agreement with observations of atmospheric absorption, *J. Clim.*, *12*, 1589–1600.

Arking, A. (1999b), The influence of clouds and water vapor on atmospheric absorption, *Geophys. Res. Lett.*, *26*, 2729–2732.

Barker H. W., et al. (2003), Assessing 1D atmospheric solar radiative transfer models: Interpretation and handling of unresolved clouds, *J. Clim.*, *16*, 2676–2699.

Berk, A., et al. (2000), MODTRAN4 user's manual, Air Force Res. Lab., Hanscom Air Force Base, Mass.

Bowker, D. E., R. E. Davis, D. L. Myrick, K. Stacy, and W. T. Jones (1985), Spectral reflectances of natural targets for use in remote sensing studies, *NASA Ref. Publ.*, *1139*.

Box, M. A., and A. Deepak (1979), Atmospheric scattering corrections to solar radiometry, *Appl. Opt.*, *18*(12), 941–949.

Bush, B. C., F. P. J. Valero, S. A. Simpson, and L. Bignone (2000), Characterization of thermal effects in pyranometers: A data correction algorithm for improved measurements of surface insolation, *J. Atmos. Oceanic Technol.*, *17*, 165–175.

Cess, R. D., et al. (1995), Absorption of solar radiation by clouds: Observation versus models, *Science*, *267*, 496–499.

Cess, R. D., M. H. Zhang, Y. Zhou, X. Jing, and V. Dvortsov (1996), Absorption of solar radiation by clouds: Interpretations of satellite, surface, and aircraft measurements, *J. Geophys. Res.*, *101*, 23,299–23,309.

Cess, R. D., T. Qian, and M. Sun (2000), Consistency tests applied to the measurement of total, direct, and diffuse shortwave radiation at the surface, *J. Geophys. Res.*, *105*, 24,881–24,887.

Charlock, T. P., and T. L. Alberta (1996), The CERES/ARM/GEWEX Experiment (CAGEX) for the retrieval of radiative fluxes with satellite data, *Bull. Am. Meteorol. Soc.*, *77*, 2673–2683.

Conant, W. C., V. Ramanathan, F. P. J. Valero, and J. Meywerk (1997), An examination of the clear-sky solar absorption over the central equatorial Pacific: Observations versus models, *J. Clim.*, *10*, 610–620.

Conant, W. C., A. M. Vogelmann, and V. Ramanathan (1998), The unexplained solar absorption and atmospheric H_2O: A direct test using clear-sky data, *Tellus, Ser. A*, *50*, 525–533.

Deepak, A., and M. A. Box (1978a), Forward scattering corrections for optical extinction in aerosol media 1: Monodispersions, *Appl. Opt.*, *17*(18), 2900–2908.

Deepak, A., and M. A. Box (1978b), Forward scattering corrections for optical extinction in aerosol media 1: Polydispersions, *Appl. Opt.*, *17*(19), 3169–3176.

De Rooij, W. A., and C. C. A. H. Van der Stap (1984), Expansion of Mie scattering matrices in generalized spherical functions, *Astron. Astrophys.*, *131*, 237–248.

Dougle, P. G., and H. M. Ten Brink (1996), Evaporative losses of ammonium nitrate in nephelometry and impactor measurements, *J. Aerosol Sci.*, *27*, S511–S512.

Dougle, P. G., J. P. Veefkind, and H. M. Ten Brink (1998), Crystallisation of mixtures of ammonium nitrate, ammonium sulphate, and soot, *J. Aerosol Sci.*, *29*, 375–386.

Dutton, E. G., J. J. Michalsky, T. Stoffel, B. W. Forgan, J. Hickey, D. W. Nelson, T. L. Alberta, and I. Reda (2001), Measurement of broadband diffuse solar irradiance using current commercial instrumentation with a correction for thermal offset errors, *J. Atmos. Oceanic Technol.*, *18*, 297–314.

Flowers, E. C., and E. L. Maxwell (1985), Characteristics of network measurements, *Sol. Cells*, *18*, 205–212.

Fouquart, Y., B. Bonnel, and V. Ramaswamy (1991), Intercomparing shortwave radiation codes for climate studies, *J. Geophys. Res.*, *96*, 8955–8968.

Fröhlich, C. (1991), History of solar radiometry and the world radiometric reference, *Metrologia*, *28*(3), 111–115.

Fröhlich, C., and J. London (1986), Revised instruction manual on radiation instruments and measurements, *Tech. Doc. WMO/TD 149*, 140 pp., World Meteorol. Org., Geneva.

Fröhlich, C., R. Philipona, J. Romero, and C. Wehrli (1995), Radiometry at the Physikalisch-Meteorologisches Observatorium Davos and World Radiation Centre, *Opt. Eng.*, *34*, 2757–2766.

Fu, Q., G. Lesins, W. Sun, and J. Higgins (1998), Downward surface diffuse solar irradiances in clear atmospheres: Comparison between model and observations, in *Proceedings of Eighth ARM Science Team Meeting, 23–27 March 1998, Tucson Arizona*, *Rep. DOE/ER0738*, pp. 271–276, U.S. Dep. of Energy, Washington, D. C.

Halthore, R. N., and S. E. Schwartz (2000), Comparison of model-estimated and measured diffuse downward irradiance at surface in cloud-free skies, *J. Geophys. Res.*, *105*, 20,165–21,077.

Halthore, R. N., S. Nemesure, S. E. Schwartz, D. G. Imre, A. Berk, E. G. Dutton, and M. H. Bergin (1998), Models overestimate diffuse clear-sky surface irradiance: A case for excess atmospheric absorption, *Geophys. Res. Lett.*, *25*(19), 3591–3594.

Hansen, A. D. A. (2002), The aethalometer, Magee Sci. Co., Berkeley, Calif.

Hansen, A. D. A., and R. C. Schnell (1991), The aethalometer, instrument manual, Magee Sci. Co., Berkeley, Calif.

Harrison, L., and J. Michalsky (1994), Objective algorithms for the retrieval of optical depths from ground-based measurements, *Appl. Opt.*, *33*, 5126–5132.

Henzing, J. S., and W. H. Knap (2001), Uncertainty in pyranometer and pyrheliometer measurements at KNMI in De Bilt, *Tech. Rep. TR-235*, 22 pp., R. Neth. Meteorol. Inst., De Bilt, Netherlands.

Henzing, J. S., W. H. Knap, P. Stammes, H. M. Ten Brink, G. P. A. Kos, A. Even, D. P. J. Swart, A. Apituley, and J. B. Bergwerff (2001), The effect of aerosol on closure of the regional short-wave radiation balance, CLOSAeR, *Global Change Rep. 410200087*, 93 pp., Natl. Inst. for Public Health and the Environ., Bilthoven, Netherlands.

Intergovernmental Panel on Climate Change (IPCC) (2001), *Climate Change 2001: The Scientific Basis, Contribution of Working Group I to the Third Assessment Report of the Intergovernmental Panel on Climate Change*, edited by J. T. Houghton et al., 881 pp., Cambridge Univ. Press, New York.

Kato, S., T. P. Ackerman, E. E. Clothiaux, J. H. Mather, G. G. Mace, M. L. Wesely, F. Murcray, and J. Michalsky (1997), Uncertainties in modeled and measured clear-sky surface shortwave irradiances, *J. Geophys. Res.*, *102*, 25,881–25,898.

Kinne, S., R. Bergstrom, O. B. Toon, E. Dutton, and M. Shiobara (1998), Clear-sky atmospheric solar transmission: An analysis based on FIRE 1991 field experiment data, *J. Geophys. Res.*, *103*, 19,709–19,720.

Klein Baltink, H., H. van der Marel, and A. G. A. van der Hoeven (2002), Integrated atmospheric water vapor estimates from a regional GPS network, *J. Geophys. Res.*, *107*(D3), 4025, doi:10.1029/2000JD000094.

Knap, W. H., and A. Los (2004), Sun photometry at the Jungfraujoch, in *Activity Report 2003*, Int. Found. High Altitude Res. Stn., Jungfraujoch and Gornergrat, Switzerland.

Kurucz, R. L. (1995), The solar irradiance by computation, in *Proceedings of the 17th Annual Review Conference on Atmospheric Transmission Models*, edited by G. P. Anderson, R. H. Picard, and J. H. Chetwynd, *Spec. Rep. 274*, 332 pp., Phillips Lab. Geophys. Dir., Hanscom Air Force Base, Mass.

Lacis, A. A., J. Chowdhary, M. I. Mischenko, and B. Cairns (1998), Modeling errors in diffuse-sky radiation: Vector versus scalar treatment, *Geophys. Res. Lett.*, *25*, 135–138.

Li, Z., and L. Moreau (1996), Alteration of atmospheric solar absorption by clouds: Simulation and observation, *J. Appl. Meteorol.*, *35*, 653–670.

Michalsky, J., E. Dutton, M. Rubes, D. Nelson, T. Stoffel, M. Wesley, M. Splitt, and J. DeLuisi (1999), Optimal measurement of surface shortwave irradiance using current instrumentation, *J. Atmos. Oceanic Technol.*, *16*, 55–69.

Mlawer, E. J., P. D. Brown, S. A. Clough, L. C. Harrison, J. J. Michalsky, P. W. Kiedron, and T. Shippert (2000), Comparison of spectral direct and diffuse solar irradiance measurements and calculations for cloud-free conditions, *Geophys. Res. Lett.*, *27*, 2653–2656.

Ohmura, A., et al. (1998), Baseline surface radiation network (BSRN/WCRP), a new precision radiometry for climate research, *Bull. Am. Meteorol. Soc.*, *79*, 2115–2136.

Pilewskie, P., and F. P. J. Valero (1995), Direct observations of excess solar absorption by clouds, *Science*, *267*, 1626–1629.

Ramanathan, V., B. Subasiler, G. J. Zhang, W. Conant, R. D. Cess, J. T. Kiehl, H. Grassl, and L. Shi (1995), Warm pool heat budget and shortwave cloud forcing: A missing physics?, *Science*, *267*, 499–503.

Seinfeld, J. H., and S. N. Pandis (1998), *Atmospheric Chemistry and Physics: From Air Pollution to Climate Change*, John Wiley, Hoboken, N. J.

Shettle, E. P., and R. W. Fenn (1979), Models for the aerosols of the lower atmosphere and the effects of humidity variations on their optical properties, *Tech. Rep. AFGL-TR-79-0214*, Air Force Geophys. Lab., Hanscom Air Force Base, Mass.

Solomon, S., R. W. Portmann, R. W. Sanders, and J. S. Daniel (1998), Absorption of solar radiation by water vapor, oxygen, and related collision pairs in the Earth's atmosphere, *J. Geophys. Res.*, *103*, 3847–3858.

Stamnes, K., S. Tsay, W. Wiscombe, and K. Jayaweera (1988), Numerically stable algorithm for discrete-ordinate-method radiative transfer in multiple scattering and emitting layered media, *Appl. Opt.*, *27*, 2502–2509.

Sunesson, A., A. Apituley, and D. P. J. Swart (1994), Differential absorption lidar system for routine monitoring of tropospheric ozone, *Appl. Opt.*, *33*, 7045–7058.

Ten Brink, H. M., J. P. Veefkind, A. Waijers-Ijpelaan, and J. C. van der Hage (1996), Aerosol light-scattering in the Netherlands, *Atmos. Environ.*, *30*, 4251–4261.

Ten Brink, H. M., A. Khlystov, G. Kos, T. Tuch, C. Roth, and W. Kreyling (2001), A high-flow humidograph for testing the water uptake by ambient aerosol, *Atmos. Environ.*, *34*, 4291–4300.

Valero, P. J., and B. C. Bush (1999), Measured and calculated clear-sky solar radiative fluxes during the Subsonic Aircraft Contrail and Cloud Effects Special Study (SUCCESS), *J. Geophys. Res.*, *104*, 27,387–27,398.

Van Pul, W. A. J., A. A. M. Holtslag, and D. P. J. Swart (1994), A comparison of ABL heights inferred routinely from lidar and radiosondes at noontime, *Boundary Layer Meteorol.*, *68*, 173–191.

Veefkind, J. P., J. C. H. van der Hage, and H. M. Ten Brink (1996), Nephelometer derived and directly measured aerosol optical depth of the atmospheric boundary layer, *Atmos. Res.*, *41*, 217–228.

Wardle, D., L. Dahlgren, K. Dehne, L. Liedquist, L. McArthur, Y. Miyake, O. Motschka, C. Velds, and C. Wells (1996), Improved measurement of solar irradiance by means of detailed pyranometer characterization, Solar heating and cooling program Task 9, *Rep. IEA-SHCP-9C-2*, 217 pp., Int. Energy Agency, Paris.

Wendisch, M., et al. (2002), Aerosol-radiation interaction in the cloudless atmosphere during LACE98: 1. Measured and calculated broadband solar and spectral surface insolations, *J. Geophys. Res.*, *107*(D21), 8124, doi:10.1029/2000JD000226.

Wesely, M. L. (1989), Parameterization of surface resistances to gaseous dry deposition in regional-scale numerical models, *Atmos. Environ.*, *23*, 1293–1304.

Wild, M. (1999), Discrepancies between model-calculated and observed shortwave atmospheric absorption in areas with high aerosol loadings, *J. Geophys. Res.*, *104*, 27,361–27,371.

Wild, M., A. Ohmura, H. Gilgen, and E. Roeckner (1995), Validation of general circulation model radiative fluxes using surface observations, *J. Clim.*, *8*, 1309–1324.

World Climate Program (WCP) (1983), World Climate Program research report of the experts meeting on aerosols and their climatic effects, Williamsburg, Virginia, 28–30 March 1983, edited by A. Deepak and H. E. Gerber, *Rep. WCP-55*, 107 pp., Geneva.

World Meteorological Organization (WMO) (1983), Guide to meteorological instruments and methods of observation, 5th ed., *Rep. WMO ISO 9060*, Geneva.

World Meteorological Organization (WMO) (1996), Guide to meteorological instruments and methods of observation, 6th ed., *Tech. Rep. WMO-TR 8*, Geneva.

Young, A. T. (1994), Air mass and refraction, *Appl. Opt.*, *33*(6), 1108–1110.

A. Apituley, J. B. Bergwerff, and D. P. J. Swart, National Institute for Public Health and the Environment (RIVM), P.O. Box 1, 3720 BA Bilthoven, Netherlands.

J. S. Henzing, W. H. Knap, and P. Stammes, Royal Netherlands Meteorological Institute (KNMI), P.O. Box 201, 3730 AE De Bilt, Netherlands. (henzing@knmi.nl; knap@knmi.nl; stammes@knmi.nl)

G. P. A. Kos and H. M. ten Brink, Energy Research Centre of the Netherlands (ECN), P.O. Box 1, 1755 ZG Petten, Netherlands.